Development of an integrated quantum light-matter interface

Bradley Mather MSci

Supervisor: Dr. Lucia Hackermüller

A Thesis submitted to the University of Nottingham for the degree of MRes (by research) Physics

School of Physics and Astronomy

University of Nottingham

October 2020

Abstract

This thesis details the work carried out to improve and develop a system capable of interfacing atoms and light through an optical fibre interface. It sports a transverse laser drilled through hole in which cold caesium-133 atoms are introduced. This system currently offers a high optical depth and the promise of scalability onto a larger waveguide chip platform. This thesis reports on the progress towards a light-matter interface, with a focus on improved fibre hole interfaces. Improved interfaces are measured which possess different hole sizes and geometries drilled into many varieties of fibres with the intention of minimising losses across the fibre hole. The fibre interface structural stability and the polarisation stability of the fibres are also measured along with fibre stability and polarisation stability. The groundwork of an EIT system implementation is also described. Finally, the preliminary analysis of a multi-waveguide photonic chip including waveguide gaps for the loading of cold atoms is presented. This work is carried out in pursuit of the longer term goal of introducing this more complex system into the main experimental chamber, replacing the fibre interface.

Contents

List of Figures

Chapter 1

Introduction

The field of cold atomic physics owes its development to the discovery and advancement of laser cooling techniques. In 1985 the first implementation of laser cooling was performed by Chu et al[1] opening the door to a whole new field of study. The newfound capability of cooling neutral atoms to the μK kelvin scale presented a host of new opportunities. The extreme temperatures which atoms can now be cooled have allowed the study of fundamental physical phenomena and previously inaccessible physical states. Most famously the prediction of a new state of matter known as the Bose-Einstein condensate (BEC) was finally shown experimentally in 1995 using ^{87}Rb[2] by Wieman and Cornell. This was made possible through the further development of cooling techniques including the magneto optical trap[3] (MOT) and evaporative cooling, bridging the gap between the Doppler cooling limit and the critical temperature needed to produce a BEC. A myriad of applications and research now exploit cold atom physics such as gravimeters[4], fundamental cosmological research[5], quantum simulators[6,7] and atomic clocks[8]. Experiments predominantly take advantage of the alkali elements such as rubidium and lithium. In this thesis, the element of interest is caesium. These materials have favourable characteristics such as low vapour pressures, relatively simple electronic structures and convenient atomic transition energies that are readily addressed by common laser diodes. These attributes make them excellent candidates for ultra-cold atomic experiments.

As a consequence of this ability to now trap and control the motion of neutral atoms with high precision, the possibility of interfacing guided light with cold atoms in a direct and controllable manner becomes positively achievable. This is

desirable for many quantum information and computing schemes[9,10,11]. When an atom or ensemble is isolated from the environment it is readily addressed by probe light which can carry quantum information. The atom itself can be used to store quantum information which is less feasible with light as it is difficult to store photons for a substantial amount of time[12]. A series of repeaters[13] interfacing atoms and light naturally arises as a solution to create a quantum information network. Hence, it becomes critical to create the strongest possible coupling between the atoms and light to elicit strong interactions, thereby realising an effective atom-photon interface for information transfer[9,14]. Interest in this area of research has surged in recent times and multiple systems have been produced which seek to produce hybrid photonic devices using waveguides[15] which integrate trapped cold atoms. Examples include systems employing hollow core fibres[16,17] and tapered nano-fibres[14,18]. Tapered nano fibres utilise the evanescent wave field produced from the waveguide waist itself, trapping atoms. Hollow core fibres on the other hand, confine both photons and atoms in their core simultaneously, facilitating interactions between the two.

In this project we continue the development of a novel implementation which currently interfaces atoms and light by introducing a transverse laser drilled void spanning the entire width of the core ($\sim 5\mu$m) of a standard single mode optical fibre (diameter of $\sim 100\mu$m). Within this void laser cooled ^{133}Cs atoms are introduced by an axial dipole trap into the drilled void. Light coupled to the fibre passes through this void which lies perpendicular to the propagation of the light, interacting with the introduced laser cooled atoms. This system has the distinct advantage of utilising much greater separation distances between the thermal surfaces of the waveguide and the cooled atomic ensemble as opposed to hollow core and tapered fibre systems. This limits problems such as the thermalisation of atoms reducing the ability to elicit quantum behaviour and interact with the atoms effectively through line-broadening of atomic transitions. Additionally, the relatively straight forward process of introducing a transverse through-hole to already industry standard optical fibres lends this technique to easy conversion of existing fibre optic information systems.

Much of the content of this thesis focuses on the improvement of this system. The first aspect investigated is the fibre interface itself. The effect of varying sizes and

geometries (circular, square and convex) of fibre holes are measured in the pursuit of greater light transmission through the fibre. Additionally, structural stability analysis and polarisation stability measurements are produced to determine the suitability of the new interfaces for insertion into the main experiment. These topics are solely the results of my efforts. We then introduce the topic of EIT (electromagnetic induced transparency), which is planned to be to the system in the near future. An initial room temperature set-up is used to elicit EIT as a proof of concept that will then be applied to the main experiment in due course, I have assisted in the data collection and analysis of this topic. Finally, preliminary testing on an advanced silica on silicon waveguide chip, which includes waveguide gaps ready for the introduction of trapped atoms is presented. This final topic is also solely my work.

1.1 Thesis overview

Overview of the contents of each chapter of the thesis:

Chapter 2 - Introduces all of the major theoretical concepts, mathematics and experimental techniques required to understand the experiment and the experimental procedures.

Chapter 3 - Provides a detailed outline of the experimental set-up of the main experiment and an explanation of the experimental procedure including all of the important components.

Chapter 4 - Presents all of the work carried out to improve the experimental system. Includes the experimental set-up, methodology and results of each test.

Chapter 5 - Concludes the thesis with the outlook of the experiment and the future steps to be taken.

Chapter 2

Alkali atoms, laser cooling and trapping techniques

To grasp the experimental techniques presented in this thesis an understanding of atomic theory is required. An outline of the relevant atomic physics will be given with a particular focus on the alkali atoms due to their significance in the field of cold atoms and their centrality to this work. Using the understanding of the atomic physics of the alkalis we will explore the various methods of laser cooling and atomic manipulation, concentrating on those techniques which are of greatest importance to our work.

2.1 The alkali atoms

The alkalis are an excellent candidate for experiments utilising cooled atomic clouds. Firstly, the alkali metals have a relatively high vapour pressure[19,20]. This is conducive to producing a reliable stream of gaseous atoms from a substrate in an UHV (ultra-high vacuum) system using a heating element. Secondly, the optical electron transitions of the alkali elements fall within an infrared frequency region which can be supplied by readily available laser diodes. This makes them a convenient choice for experiments involving laser cooling.

Most importantly is the signature property of the alkalis, that being their single valence electron. This property allows us to approximate the atom's electronic structure by way of the Hydrogen atom as the complete atomic shells of the alkalis contribute a net angular momentum of zero. The filled electron sub shells

below that of the valence electron have large excitation energies and so simplify the atomic energy level structure when dealing with electron transitions and concentrate on the lone valence electron. The first instance of laser cooling or deceleration using photons incorporated Mg^+ ions[21], which replicate the structure of the alkalis with only one valence electron, their second electron having been removed. Laser cooling then quickly moved on to incorporate the alkali metals with Na atoms used first[22].

As the alkali atom's can be said to have a pseudo-hydrogenic structure the central field approximation can be used to simplify their analysis[23]. This is a good starting point but there are multiple effects which need to be factored in to produce a good model for the electronic energy level structure. Of particular interest for this work is caesium. By incorporating these effects into our model we will arrive at the specific dipole transitions which will be pertinent to the photon emission and absorption from caesium in our experiments. The central field approximation can be used for caesium as its alkali structure means we can model it as a hydrogen-like atom with a central positive charge and a single valence electron and treating its filled shells effectively as shielding. This approximation can be described using the Schrödinger equation,

$$\left[\frac{-\hbar^2}{2m_e}\nabla + V_{\text{eff}}(r) \right] \psi = E\psi \tag{2.1}$$

where m_e denotes the mass of the electron, ψ the wave function, E the energy of the system and V_{eff}, which is the effective central potential, accounting for the electron shielding present in the alkalis. Furthermore, the Hamiltonian for our system is given by,

$$\hat{H}_o = \frac{\hat{P}^2}{2m_e} + V_{\text{eff}}(r) \tag{2.2}$$

where $\hat{P}$ represents the momentum operator for the outermost electron. To gain an understanding of the electronic structure of caesium sufficient to find the electron transitions relevant to our experiment, we must introduce a few corrections to our simplistic central field approximation. Only the important steps and results will be presented here to provide a theoretical base as a thorough derivation lies outside the scope of this thesis and can be found in many academic resources[20,23,24].

The first correction to our model gives us the fine structure of an atom. This correction takes into account the relativistic speed of the electron's orbits around the atomic nucleus. It also incorporates the spin-orbit coupling of the electron's intrinsic magnetic moment and the magnetic field generated by the electron's orbital angular momentum. Performing a Taylor expansion on the relativistic energy of the electron yields:

$$E_e = \sqrt{p^2c^2 + m_e^2c^4} \approx m_e^2c + \frac{1}{2}\frac{p^2}{m_e} - \frac{1}{8}\frac{p^4}{m_e^3c^2} \tag{2.3}$$

where p is the momentum of the electron and c is the speed of light. The first three terms characterise the rest energy, the kinetic energy for non-relativistic speeds and the final term provides the initial term for the relativistic speed correction of the electron respectively. We can then treat this as a perturbation for our Hamiltonian,

$$\hat{H}' = -\frac{\hat{p}^4}{8m_e^3c^2}. \tag{2.4}$$

By then employing perturbation theory we can reach a first order energy correction according to the relativistic velocity of the electron[25],

$$E_n^{(1)'} = -\frac{(E_n)^2}{2m_ec^2}\left[\frac{4n}{l + \frac{1}{2}} - 3\right] \tag{2.5}$$

where n is the principal quantum number and l is the orbital angular momentum quantum number.

An added layer of complexity arises once again due to the motion of the electron. The intrinsic magnetic moment of the electron interacts with the magnetic field produced by it's own orbital movement. This is know as the spin-orbit interaction and coupled with the relativistic correction (both effects are on the same order of magnitude) produces the fine structure of the electron energy levels. The Hamiltonian of this corrective perturbation can be produced by combining the spin magnetic moment of the electron and the magnetic field via the Biot-Savart law,

$$H_{so}' = -\boldsymbol{\mu_s} \cdot \boldsymbol{B_l} = \frac{g_s\mu_B}{2\hbar}\boldsymbol{S}\cdot\boldsymbol{L}\frac{\mu_o e}{4\pi r^3 m_e} = \frac{\mu_o e^2}{8\pi m_e^2 r^3}\boldsymbol{S}\cdot\boldsymbol{L}. \tag{2.6}$$

Our spin-orbit interaction Hamiltonian is produced via a dot product between the spin magnetic moment of the electron, $\boldsymbol{\mu_s}$, and the magnetic field produced by the angular momentum of the electron, $\boldsymbol{B_l}$. $\boldsymbol{S}$ and $\boldsymbol{L}$ represent the spin and orbital angular momentum operators respectively. We also use the g-factor for the electron g_s, the vacuum permeability constant μ_o and the Bohr magneton, μ_B. To continue it is helpful to define the total angular momentum, such that,

$$\boldsymbol{J} = \boldsymbol{L} \cdot \boldsymbol{S} \tag{2.7}$$

where the Value of $\boldsymbol{J}$ can take the values between,

$$|L - S| \leq J \leq L + S \tag{2.8}$$

in integer steps. The spin-orbit coupling term can be expanded[24],

$$\boldsymbol{L} \cdot \boldsymbol{S} = \frac{1}{2}\hbar^2 \left[j(j+1) - l(l+1) - s(s+1) \right] \tag{2.9}$$

and defining a spin-orbit coupling constant as,

$$a_{so} = \frac{\mu_o e^2 \hbar^2}{8\pi m_e^2 r^3} \tag{2.10}$$

We can then rewrite our Hamiltonian as,

$$H'_{so} = \frac{a_{so}}{2} \left[j(j+1) - l(l+1) - s(s+1) \right] \tag{2.11}$$

The eigenstates of our Hamiltonian have the basis $|n, s, l, j, m_j\rangle$ which satisfactorily define the electron state. Using perturbation theory again, we find an expression for the energy shift due to the spin orbit correction,

$$\triangle E = -\frac{E_n}{2n}\alpha^2 \frac{j(j+1) - (l+1) - \frac{3}{4}}{l(l + \frac{1}{2}(l+1))} \tag{2.12}$$

By combining the relativistic effects and the spin-orbit correction we get to an expression for the fine structure of a simple hydrogen atom[25],

$$E_{n,j} = E_n \left[1 + \frac{\alpha^2}{n} \left(\frac{1}{j + \frac{1}{2}} - \frac{3}{4n} \right) \right] \tag{2.13}$$

where we have inserted the fine structure constant $\alpha \approx \frac{1}{137}$ for convenience and n simply represents the principal quantum number.

We can go further and find an expression for the hyperfine structure of the atom which further splits the possible atomic energy levels. This level of precision is most important for the photonic interactions with caesium's electronic structure which will be discussed later - they are a crucial component of the experimental work presented. The hyperfine structure takes into account the nucleus of the atom, the magnetic moment of the nucleus, $\boldsymbol{I}$, interacts with the electron's total angular momentum $\boldsymbol{J}$. Similar to the spin-orbit interaction it is helpful to define a new quantum number known as the atomic angular momentum,

$$\boldsymbol{F} = \boldsymbol{J} + \boldsymbol{I} = \boldsymbol{L} + \boldsymbol{S} + \boldsymbol{I} \tag{2.14}$$

where $\boldsymbol{F}$ can take on the values between,

$$|J - I| \leq F \leq J + I \tag{2.15}$$

in integer steps. The number of hyperfine level splittings is defined by the $2F+1$ sub levels. However, these levels are degenerate until an external magnetic field perturbs the atom[20]. The Hamiltonian describing the hyperfine interaction without the added complexity or an external magnetic field takes the form[20]

$$H_{\text{hfs}} = A_{\text{hfs}}\boldsymbol{I} \cdot \boldsymbol{J} \tag{2.16}$$

where A_{hfs} is the magnetic dipole constant. The eigenstates of the Hamiltonian have the basis $|n, s, l, j, i, f, m_f\rangle$, however as mentioned previously the splitting will not depend on m_f until the degeneracy is broken by an external magnetic field.
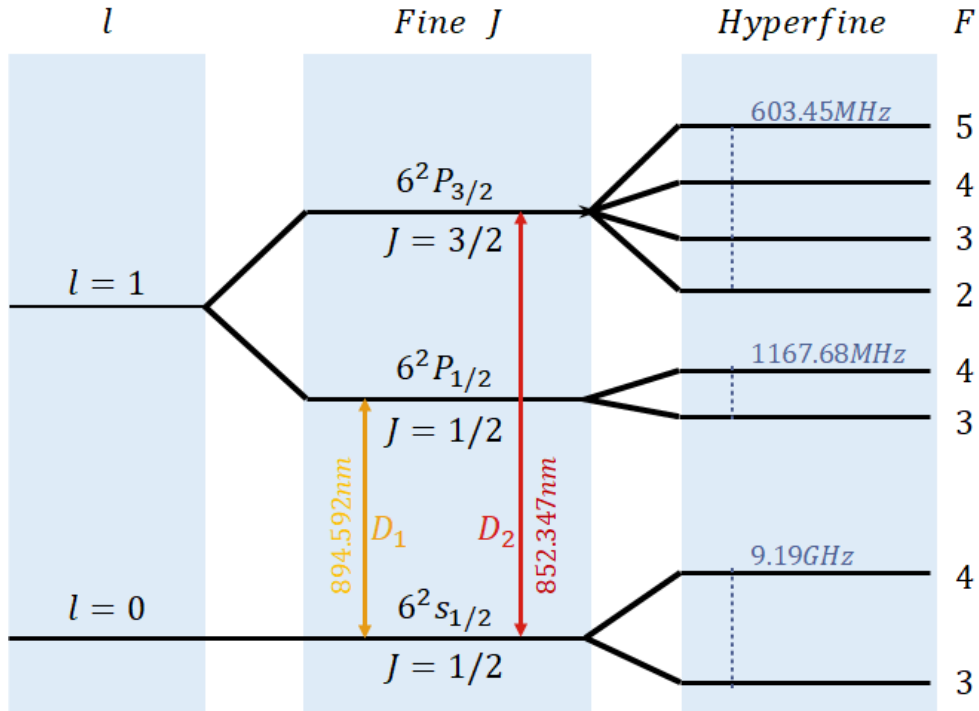
Figure 2.1: Energy level diagram for caesium including the fine and hyperfine structures in vacuum. Each level is labelled by its spectroscopic notation and frequency bands across the hyperfine are given for reference, the splitting is not to scale. The D_1 and D_2 transitions are clearly labelled with their associated wavelengths. For more detailed information see [20].

The overall picture of the electron energy level structure of [133]Cs can be seen in figure 2.1. This diagram shows the level splitting as described throughout this section, taking into account the fine and hyperfine structure. From left to right we see a branching structure, which shows the splitting of the electron energy levels due to progressively weaker interactions. The ground state of the valence electron of caesium occupies an s-orbital where $l = 0$. The fine structure can only take on a $J = 1/2$ value according to equation 2.8, this then splits into a doublet manifold of $F = 3, 4$ owing to caesium's nuclear angular momentum of $I = 7/2$ and using equation 2.15. The same analysis holds true for the excited state of the valance electron which will occupy a p-orbital where $l = 1$. The fine structure can then take on two values where $J = 1/2, 3/2$ according to equation 2.8. The $J = 3/2$ state can then split into a 4 way manifold of $F = 2, 3, 4, 5$ according to equation 2.15.

Spectroscopic notation is commonly used to indicate transitions such as the D_2 line displayed in figure 2.1, which can be written as $6^2S_{1/2} \rightarrow 6^2P_{3/2}$. Here the first number indicates the principal quantum number of the valence electron, the

superscript indicates the multiplicity of the state, the letter indicates the orbital quantum number $(S, P, D \rightarrow l = 0, 1, 2$ respectively) and the subscript gives the total angular quantum number, J.

2.1.1 Interactions with magnetic fields

Magnetic fields are frequently used to manipulate atoms during experiments, it is therefore important to understand the interaction which occurs and how it affects the energy level structure. Applied magnetic fields further split the energy level structure past that of the fine structure splitting and hyperfine splitting. This splitting breaks the degeneracy in the m_F levels and is known as the Zeeman effect. The magnitude of the splitting increases with magnetic field strength.

When a magnetic field is introduced the interaction Hamiltonian becomes,

$$H_b = -\boldsymbol{\mu} \cdot \boldsymbol{B} \qquad (2.17)$$

where $\boldsymbol{B}$ represents the magnetic field and the atomic magnetic dipole is given by,

$$\boldsymbol{\mu_{atom}} = -g_J \mu_B \boldsymbol{J} + g_I \mu_N \boldsymbol{I} \approx -g_J \mu_B \boldsymbol{J} \qquad (2.18)$$

Here, g_J and g_I are the g-factors for the electron and nucleus respectively and hence we can show that for a weakly perturbing magnetic field $(\mu_B < A_{\mathrm{hfs}})$[23],

$$H_b = g_F \mu_B \boldsymbol{F} \cdot \boldsymbol{B} = g_F \mu_B B F_z \qquad (2.19)$$

where we define the Landé factor,

$$g_F = \frac{F(F + 1) + J(J + 1) + I(I + 1)}{2F(F + 1)} g_J. \qquad (2.20)$$

Therefore, in a weakly perturbing magnetic field we break the degeneracy of the hyperfine structure leading to splitting of the energy levels with spacing of[23],

$$\triangle E_{hfs} = g_F \mu_B m_f B \qquad (2.21)$$

this phenomena is known as the anomalous Zeeman effect[23]. There are regimes at which the hyperfine splitting and the magnetic field strength are similar, or where the magnetic field strength is dominant and the hyperfine correction is

treated as the perturbation, this however, lies outside the scope of this thesis but is fully detailed here[23].

2.1.2 Interactions with electric fields

The laser is an indispensable tool in the field of cold atom physics. The device is used in practically every aspect of our experiments including probing, imaging, atom cooling and atomic state preparation. It is therefore key to understand how the electric fields (and equally photons) we employed in experiments interact with the atomic species.

The interaction between atoms and light can be simplified to a familiar two-level quantum system which is then treated semi-classically by applying an oscillating electric field[23,24]. An external electric field of the form,

$$\boldsymbol{E} = \boldsymbol{E_o}\cos(\omega t) \tag{2.22}$$

will act upon atoms which we can model to behave like an electric dipole. Neutral atoms can be acted upon by electric fields owing to the instantaneous charge distribution within atoms which is characterised by α, the polarisability. Therefore the induced dipole moment established by the electric field on an atom is,

$$\boldsymbol{p} = \alpha\boldsymbol{E} \tag{2.23}$$

This interaction results in two forces acting on the atom, which can be added as such,

$$\boldsymbol{F_{\text{tot}}} = \boldsymbol{F_{\text{scat}}} + \boldsymbol{F_{\text{dip}}}. \tag{2.24}$$

The scattering force acts similarly to the classical conception, by which photons of light impart momentum to the atom in the direction of the photon. The dipole force occurs as a result of the electric field's intensity gradient, whereby the atom is attracted towards the most intense part of the field (assuming the atom has a refractive index greater than the surrounding medium). Both of these forces are important for providing control of atoms during an experiment.

A Hamiltonian can be defined for our semi-classical model. It is comprised of the

sum of the unperturbed Hamiltonian (equation 2.2) defining the energy levels of the atom and the second part of the Hamiltonian which represents the applied electric field and can be retrieved by combining equations 2.22 and 2.23:

$$H_{tot} = H_o + H_E(t) = H_o - \alpha E_o cos(\omega t) \qquad (2.25)$$

Our model describes an atom with two levels, a ground state $|0\rangle$ and an excited state $|1\rangle$ with an energy transition of $\hbar\omega_o$, where ω_o is defined as the resonant frequency for the transition. We begin with a typical wavefunction associated with H_o expressing energy levels E_n,

$$\psi_n(\boldsymbol{r}, t) = \Psi_n(\boldsymbol{r})e^{-iE_n t/\hbar}. \qquad (2.26)$$

For a two-level system only a ground and an excited level are taken into account[1],

$$\sum_{j=0,1} H_o\Psi_j(\boldsymbol{r}) = \sum_{j=0,1} E_j\Psi_j(\boldsymbol{r}) \qquad (2.27)$$

We can express our wavefunctions more concisely in Dirac notation,

$$\sum_{j=0,1} \Psi_j(\boldsymbol{r}, t) = \sum_{j=0,1} c_j \, |j\rangle \, e^{-i\omega_j t} \qquad (2.28)$$

We have also removed the time dependence label from the probability amplitudes, c_0 and c_1, and define $\omega_j = E_j/\hbar$. Normalisation of our wavefunction requires that our two time dependent probability amplitude coefficients associated with each eigenstate satisfy $|c_0|^2 + |c_1|^2 = 1$. To introduce the perturbing electric field we use the second term from equation 2.25 along with our wavefunction for equation 2.28 and insert them into the time dependent Schrödinger equation (TDSE). This gives rise to two differential equations known as the optical Bloch equations,

$$\begin{aligned} i\dot{c_1} &= \Omega cos(\omega t)e^{-i\omega_o t}c_2 \\ i\dot{c_2} &= \Omega cos(\omega t)e^{i\omega_o t}c_1 \end{aligned} \qquad (2.29)$$

in which Ω is defined as the Rabi frequency and $\omega_o = (E_1 - E_0)/\hbar$, which is the resonant frequency of the transition. It is useful to introduce the density matrix where elements, ρ_{00} and ρ_{11}, give the populations of the ground and excited states respectively.

---

[1]The index j is used here so as to not cause confusion with the imaginary unit i.

$$\rho = \begin{pmatrix} \rho_{00} & \rho_{01} \\ \rho_{10} & \rho_{11} \end{pmatrix} \tag{2.30}$$

These terms can be found via the steady state solutions to the optical Bloch equations[23]. With a natural decay rate of the excited state, Γ_{dec} defined, the probability for an atom to be found in the excited state as t tends to infinity becomes,

$$\rho_{11} = \frac{\Omega^2/4}{\delta^2 + \Omega^2/2 + \Gamma_{dec}^2/4}. \tag{2.31}$$

Here, δ is the detuning of the electric field from the atomic transition frequency, $\delta = \omega - \omega_o$. This expression can be re-written by introducing a saturation parameter s_o and relating the Rabi frequency to the applied field,

$$s_o = \frac{I}{I_{sat}} \tag{2.32}$$

$$\Omega^2 = \frac{\Gamma_{dec}^2 I}{2 I_{sat}} \tag{2.33}$$

Where I_{sat} is the saturation intensity and I is the field intensity. Therefore the excited state expression becomes[24],

$$\rho_{11} = \frac{s_o/2}{1 + s_o + 4\delta^2/\Gamma_{dec}^2} \tag{2.34}$$

At the limit of a very intense resonant electric field the population of the excited and ground states approach 1/2, this is known as the saturation point. A lower saturation parameter will lead to a greater ground state population. The scattering force term first seen in equation 2.24 can then be expressed as the average force due to inbound photons striking the atom,

$$\langle F_{scat} \rangle = \hbar \boldsymbol{k} \Gamma_{scat} \tag{2.35}$$

where the photon scattering rate is defined as $\Gamma_{scat} = \Gamma_{dec} \rho_{11}$. The absorption of a photon imparts a quantum of momentum, $\boldsymbol{p} = \hbar \boldsymbol{k}$, where k is the wavevector of the photon. This raises an electron in the atom to its excited state. At a later time spontaneous photon emission in a random direction will impart momentum to the atom opposite the photon's direction of emission bringing it back to its ground state. Hence the scattering force is considered directional only over an average number of photon absorptions and emissions. The momentum imparted

via absorption is always directional when induced by a laser and the random emissions which take the atom back to its ground state will produce a zero net movement when summed over many cycles.
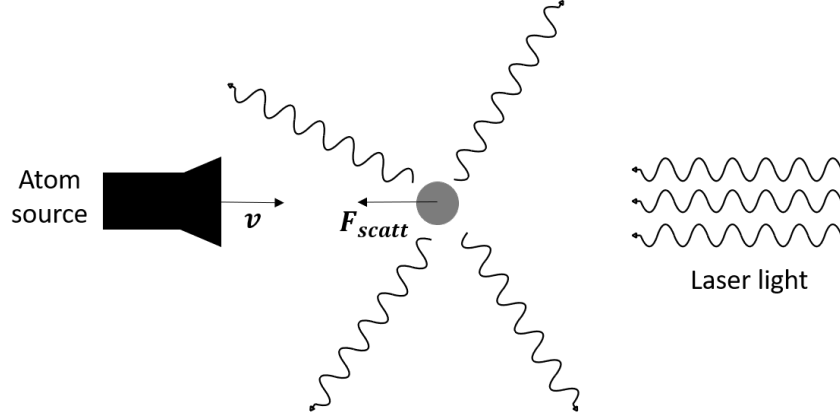
Figure 2.2: This diagram shows the simple interaction in which atoms of velocity v stream out of a source and are slowed by oncoming laser light. The scattering force F_{scatt} and its direction is shown. Photons leaving the atom are from spontaneous emission and are isotropic.

The use of lasers to direct photons at atoms, imparting momentum and hence controlling their direction, velocity, kinetic energy and therefore temperature is of great importance to the cold atom field. We will see in section 2.3 how we use lasers to cool atoms and create magneto optical traps (MOTs). The limit to the deceleration our lasers can impose on atoms can be expressed in several forms[23],

$$a_{max} = \frac{\langle F_{scat}\rangle_{max}}{M} = \frac{\hbar k \Gamma_{dec}}{2M} = \frac{v_r}{2\tau} \tag{2.36}$$

where M is the atomic mass, v_r is the recoil velocity of the atom during a photon emission or absorption event and τ is the lifetime of the excited state. These expressions are valid in the limit where the radiation intensity, $I \gg I_s$, the saturation intensity and the values of the excited and ground state approach 1/2. The dipole force term from equation 2.24 can also now be expressed as,

$$\boldsymbol{F_{dip}} = -\frac{\hbar\delta}{2}\frac{\Omega}{\delta^2 + \Omega^2/2 + \Gamma_{dec}^2/4}\nabla\Omega \tag{2.37}$$

The dipole trap plays a pivotal role in the experiment presented in this thesis, the implementation in the experimental work can be seen in chapter 3 and further theoretical formulation can be found in section 2.4.

2.2 Laser cooling

All laser cooling processes exploit the interactions between neutral atoms and electric fields. The theory presented in section 2.1.2 provides the mechanisms by which these interactions take place and are key to understand the various methods which constitute laser cooling. The scattering force interaction as seen previously applies radiative pressure via laser light. It is this aspect of equation 2.24 which we will focus on in this section. By imparting momentum via photon absorption the velocity of atoms can be reduced along with their their kinetic energy and hence an ensemble of atoms can be slowed then together with the magnetic field also "cooled."

Doppler cooling

The scattering force of light set out so far allows us to apply a radiative force upon atoms but does not generate an overall cooling effect. To cool atoms we need to reduce the spread of the velocity distribution and hence we require our cooling process to be velocity selective. Such processes were suggested by Wineland, Dehmelt, Hansch, Schawlow and Itano[26,27,28]. Fortunately, this can be achieved thanks to the highly frequency dependent nature of atomic photon absorption at resonance. This frequency dependence consequently allows us to make absorption velocity dependent by exploiting the Doppler shift effect, which occurs as the frequency of light 'seen' by atoms is shifted in the atoms reference frame relative to a stationary light source. An atom moving towards a light source of resonant light will see blue-shifted and therefore off-resonance detuned light. By deliberately red-detuning the light, the photons will resonate with atoms moving towards the light source (the atom and the light counter-propagate).

We can define the scattering rate equation[24] taking into account the Doppler shift, which is defined as $\omega_D = -\boldsymbol{k} \cdot \boldsymbol{v}$,

$$\Gamma_{scat} = \frac{s_o \Gamma_{dec}/2}{1 + s_o + [2(\delta + \omega_D)/\Gamma_{dec}]^2}. \tag{2.38}$$

Equations 2.35 and 2.36 can then be used to find the average scattering force and the maximum deceleration according to the Doppler shift by substituting for Γ_{scat}.

The slowing effect imparted on atoms by this constant frequency approach is limited. The Doppler cooling method requires that photon absorption must be highly frequency selective around the resonant frequency. However, this becomes a problem as the atoms decelerate and they see a red-shifted laser frequency which is no longer resonant. This is occurs when the Doppler shift has decreased by a few times the power broadened width[24], $\Gamma'_{dec} = \Gamma_{dec}\sqrt{1 + s_o}$, where the velocity change, $\triangle v$, is of the order of m/s. There are a few methods to remedy this, one is the use of laser frequency scanning such that the laser can be tuned to resonate progressively as the atoms decelerate[23]. Another method employs a spatially varying magnetic field gradient which affects the energy levels of the atoms through Zeeman splitting (see section 2.1.1). As the atoms decelerate the laser light will become red-shifted and so to maintain resonance the splitting of the energy levels will need to reduce and hence the applied magnetic field reduces along the path of the atoms.

Molasses

Doppler cooling has so far been discussed within the framework of atom-photon interactions whereby a single laser beam slows a stream of propagating atoms. The Doppler cooling method can be taken further by adding additional beams. The simplest extension to this involves a retro-reflecting mirror which reflects the original laser beam back on itself creating a counter-propagating beam, which conveniently has the same intensity, frequency and polarisation. The scattering force produced by these beams would of course become zero for atoms at rest. Light which is red-detuned with respect to the atom's resonant frequency will be seen as blue-shifted by atoms moving against the beam bringing the atom towards resonance with the light.. The reflected light will be purposefully red-shifted initially via laser tuning and then doubly so for atoms moving within the reflected beam and therefore further red-shifting the light off resonance. However, atoms moving towards the reflected beam will be on resonance and so absorbed. In effect, atoms will interact and therefore decelerate more strongly with the beam that opposes their velocity, this is what gave rise to the term 'optical molasses'[29,30]. The molasses force acting on an atom between two counter-propagating laser beams can be derived as such[23],

$$F_{\text{molasses}} = F_{scatt}(\omega - \omega_o - kv) - F_{scatt}(\omega - \omega_o + kv)$$

$$\approx F_{scatt}(\omega - \omega_o) - kv\frac{\partial F_{scatt}}{\partial \omega} - F_{scatt}(\omega - \omega_o) - kv\frac{\partial F_{scatt}}{\partial \omega} \qquad (2.39)$$

$$\approx -2\frac{\partial F_{scatt}}{\partial \omega}kv$$

in the limit of low velocities, $kv \ll \Gamma_{dec}$.
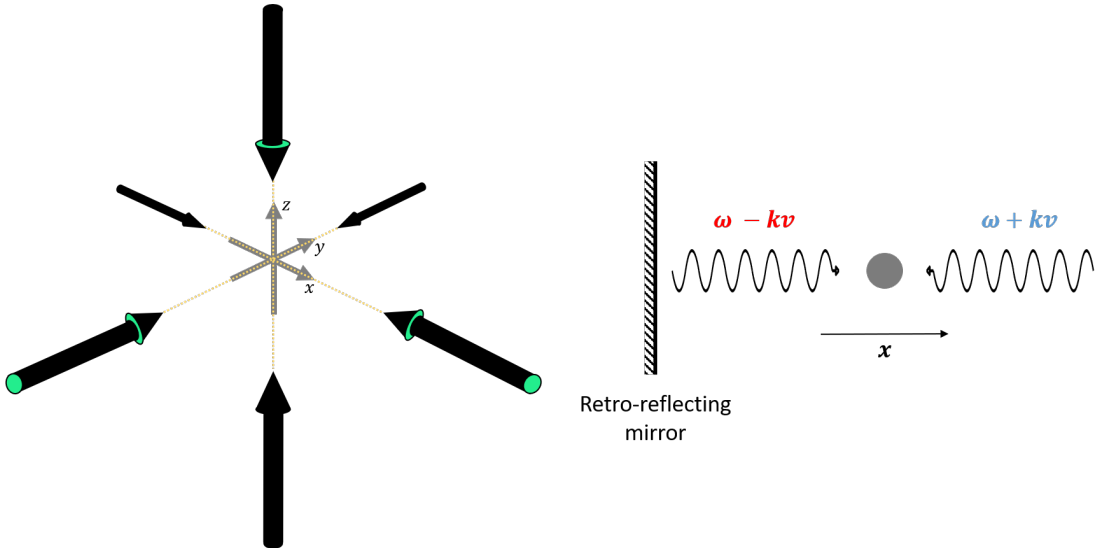
Figure 2.3: The left shows 3 pairs of counter-propagating orthogonal beams creating an optical molasses system. The right hand side shows a blue-shifted photon and a retro-reflected red-shifted photon moving towards an atom along the x direction. The use of a retro-reflecting mirror to give the co-propagating second beam for optical molasses is a common and elegant method.

A common set-up employed in experiments utilises 3 pairs of counter-propagating beams along each of the Cartesian axes (see figure 2.3). This creates a central region at the intersection of all six beams where atoms can be cooled in three dimensions. It must be noted that this three dimensional cooling method will cool an atomic cloud but will not create a trap[19]. This is due to the lack of a restoring force in the system, atoms which leave the central region via fluctuations can not be retrieved.

The limit to Doppler cooling is a consequence of the emission-absorption cycle itself. Cooling occurs as the subsequent photon emissions occur isotropically leading to a net force of zero. However, these fluctuations become important as atoms get very cold. Over time, the random walks performed by individual atoms from spontaneous emissions will inevitably lead atoms outside of the beam

intersection point. The cooling limit is defined by the Doppler temperature, which is calculated by the equilibrium point between the heating and cooling effects of the lasers,

$$T_D = \frac{\hbar\Gamma}{2k_B} \tag{2.40}$$

where k_B is the Boltzmann constant, a full derivation can be found here[23]. For the element of most interest to us, caesium, its Doppler temperature is 125μK when using the D_2 line transition as the resonant frequency[20].

The Doppler limit should theoretically apply to simple Doppler cooling and the molasses technique of multiple co-propagating beams. However, experimental evidence shows that the optical molasses technique is in fact a sub-Doppler technique. Experimentalists were pleasantly surprised when it was discovered that the molasses cooling technique could produce temperatures far lower than was calculated[31]. It turns out that the simplifying assumption of an atomic two-level system did not fully capture the physics of the technique[23]. The multiple degenerate sub levels seen in section 2.1, can be used intentionally to create even colder atomic clouds through newer sub-Doppler cooling techniques such as Sisyphus cooling[32], however these techniques lay outside the relevant scope of this thesis.

Evaporative cooling

An important technique which can cool below the Doppler limit is evaporative cooling. Although not strictly a laser cooling technique itself, it is a process used towards the end of a laser cooling procedure. The process is simple, a cooled atomic cloud of atoms will still have a distribution of thermal energies associated with it such that[23],

$$N(E) = N_o \exp\left(\frac{-E}{k_B T}\right) \tag{2.41}$$

which is the Boltzmann distribution and k_B is the Boltzmann constant, T is the temperature and N_o is the atom number. By deliberately allowing the most energetic atoms within our cooled atomic ensemble to escape the overall energy of the system is reduced and therefore it is cooled[24,33]. By doing this we cool the atoms and increase the phase-space density at the expense of atom number. Figure 2.4 shows atoms trapped in a harmonic potential. By reducing the height

of the harmonic potential the more energetic atoms are free to escape. This lowers the average kinetic energy of the remaining atoms leading to a reduced temperature, $T_2 < T_1$.
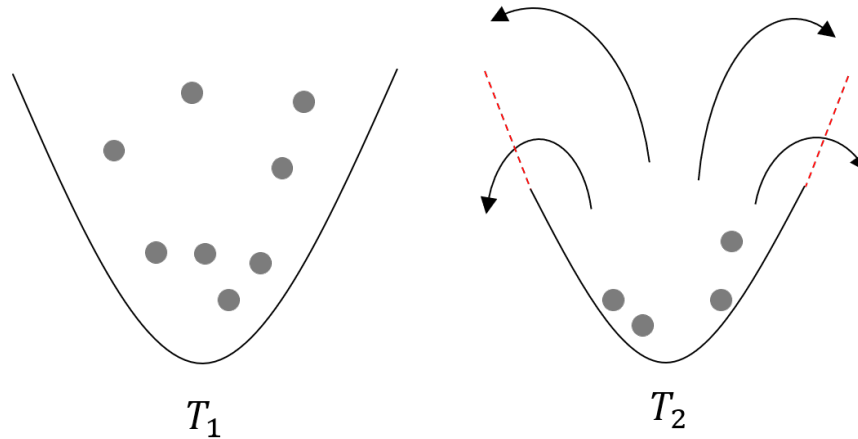
Figure 2.4: Cooled atoms lay within a harmonic potential at temperature T_1. At a later time the potential is lowered allowing the more energetic atoms higher in the potential to escape. The reduced trap depth is shown by the dashed red lines and the arrows show the more energetic atoms escaping. As a result the remaining atoms have a reduced average temperature of T_2.

2.3   Magneto-optical trap (MOT)

The molasses cooling technique described in section 2.2 is only effective at cooling neutral atoms to the μK regime due to atoms falling out of resonance. Additionally, this method does not trap atoms as it provides no restoring force to prevent atoms escaping the cooled cloud of atoms. The 3 dimensional molasses scheme can be readily transformed into an atomic trap by using a magnetic field and carefully choosing the polarisation of each beam. The magneto-optical trap or MOT is then referred to as such as it combines the optical dampening of molasses with a magnetic field to bring about a spatial trap.

A MOT requires a quadrupolar magnetic field which can be created by a pair of coils in an anti-Helmholtz configuration as seen in figure 2.5. The magnetic field cancels at the centre of the trap coinciding with intersection of all six beams. The field then increases linearly with distance away from the central region. The energy level of the excited sate of the atom, $|1\rangle$, is split under the influence of the quadrupolar field creating the three sub-levels, $M_j = -1, 0, +1$, via the Zeeman effect. The splittings can be seen in figure 2.5 along with the reversal of the

energy moving from a negative to the positive region of the magnetic field.

The energy level diagram in figure 2.5 shows the linear perturbation on the excited state sub-levels spatially along z created by the magnetic field. Here the absorption of a photon is a simple $J = 0$ to $J = 1$ transition from the ground state $|0\rangle$ to the excited state $|1\rangle$. The resonant atomic frequency can be seen at the sub-level $M_j = 0$, and the frequency associated with that energy is ω_o. As we already have seen the radiative force imparted by velocity selective cooling required a red-detuned laser to select counter-propagating atoms and slow them. This energy level can be seen in figure 2.5 as $E = \hbar\omega$ where the detuning from resonance is δ. For a photon to be absorbed it must be resonant with the atomic transition. The Zeeman splitting generates a spatially dependent energy level change so that the sub-levels $M_j = $ -1 and $M_j = +1$ move towards the supplied red-detuned light represented by the dotted line in figure 2.5.
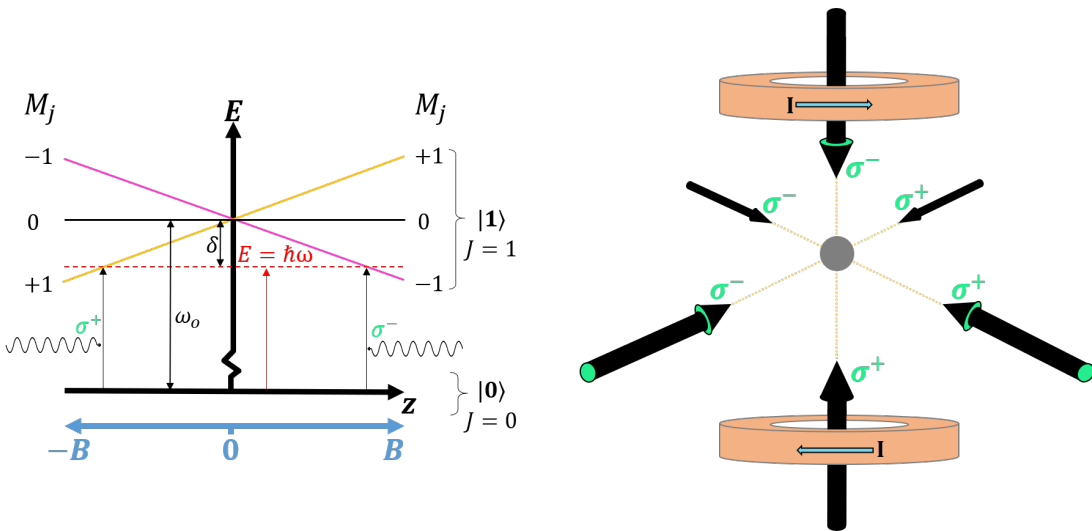
Figure 2.5: On the left hand side: a diagram representing the variation of the energy levels of the ground and excited state of an atom along the z direction. The blue arrows represent the magnetic field strength along Z. The orange and pink lines show the linearly dependent Zeeman splitting of the $M_J = +1, -1$ respectively, with $M_J = 0$ as a black line. Photons of σ^+ and σ^- polarised light travel towards $z = 0$ from the left and the right respectively. The detuning from resonance of the atomic transition (ω_o) for the re-shifted laser light is shown by δ. The energy level of the laser light used is shown with frequency, ω. On the right hand side: the set-up required to produce a MOT. A pair of coils in an anti-Helmholtz configuration (arrows indicate direction of current flow, I) surrounding a central region where $B = 0$. Three pairs of orthogonal counter-propagating beams, each pair requiring circularly polarised light, one left handed and one right.

For the Zeeman shift to create an imbalance in the radiative force and thereby create an atomic trap the polarisation of each beam must be carefully selected.

Considering the level $M_j = -1$, we can see that as an atom moves along positive z we reach resonance with our red-detuned light with frequency ω. For this transition to occur we must satisfy the selection rule for the transition $J = 0 \rightarrow M_J = -1$ by applying σ^- light. Equally, $J = 0 \rightarrow M_J = +1$ requires σ^+ light. We require that for each orthogonal beam pair a right hand circularly polarised beam and a counter-propagating left hand circularly polarised beam, represented by $\sigma^\pm$. In this way we create a spatially dependent restoring force which traps atoms whilst still applying the velocity dependent optical molasses force, trapping and cooling simultaneously.

The force acting on atoms in a magneto-optical trap can be found similarly to equation 2.39,

$$
\begin{aligned}
F_{\text{MOT}} &= F_{\text{scatt}}^{\sigma^+}(\omega - \omega_o - kv - z) - F_{\text{scatt}}^{\sigma^-}(\omega - \omega_o + kv + z) \\
&\approx -2\frac{\partial F}{\partial \omega}kv + 2\frac{\partial F}{\partial \omega_o}z
\end{aligned}
\tag{2.42}
$$

where, $\omega_o \pm z$ are the resonant absorption frequencies for the Zeeman sub-levels $M_j = \pm 1$. The Zeeman shift at a given distance is given by,

$$
\beta z = \frac{g\mu_B}{\hbar}\frac{dB}{dz}z
\tag{2.43}
$$

The force can then be expressed as,

$$
\begin{aligned}
F_{\text{MOT}} &= -2\frac{\partial F}{\partial \omega}(kv + \beta z) \\
&= -\alpha v - \frac{\alpha\beta}{k}z
\end{aligned}
\tag{2.44}
$$

This is the same result as equation 2.39 for molasses with the added restoring force introduced by the MOT and hence creating a trap as well as cooling. The spring constant of the restoring force takes the form α/z. This result can be applied to all three axis of the experiment producing a three dimensional trap.

2.4 Dipole trap

The optical dipole trap plays an important role in our experiment and so we will delve deeper into the physics of dipole force, which we first touched upon in section 2.1.2. As seen in equation 2.24 the force applied to an atom by an

electric field can be expressed as the summation of F_{scatt} and F_{dip}. We have seen the uses of the radiative pressure given by F_{scatt} in Doppler cooling and optical molasses. The dipole force term, F_{dip}, arises from the refractive property of electromagnetic radiation instead of the absorptive effects responsible for the scattering force. A beam of light with an intensity gradient (such as in figure 2.6) will apply a differential force across it's width on an atom with refractive index η. For a laser beam with a Gaussian intensity distribution the central part of the beam along its axis will have the greatest intensity. An atom in this beam will feel a differential force across it as the refraction of the higher intensity radiation from the centre imposes a greater force inward than the refraction of the lower intensity radiation imposes outward. This can be described by the simple force-potential relationship for a conservative force[23],

$$\boldsymbol{F}_{dip} = -\boldsymbol{\nabla} U_E \tag{2.45}$$

where U_E is the potential created by the electric field. This mechanism has been used to manipulate atoms and microscopic particles and is referred to as optical tweezers[34]. The applications of this technique are numerous[35], the ability to spatially control extremely small particles and atoms with high precision is incredibly useful. One example is the work done with bacteria in which the tail like appendage called the flagellum is used to propel the organism. By attaching one side of the organism to a surface the researchers were able to manipulate the organism with optical tweezers and calculate the force production generated to 'swim'[36]. The dipole beam utilised in our experiment is required for the purpose of moving tightly confined atoms through a microscopic cavity. By implementing a lens it is possible to focus a laser beam tightly and hence create an even stronger gradient force, producing a more confined trap region.
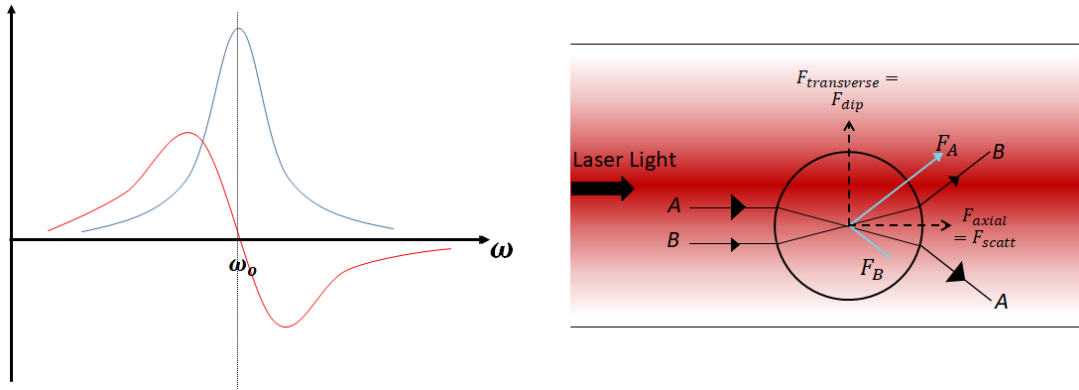
Figure 2.6: Left hand side: graph showing the absorption and refractive index characteristic of an atom across a range of frequencies centred at atomic resonance ω_o (figure adapted from[23]). The red line gives the refractive index and the blue line the absorption. Right hand side: the forces applied to an atom in a laser field exhibiting a Gaussian intensity distribution - the most intense region at the centre. Two hypothetical light rays, A and B, penetrate the atom where $A > B$. The refractive index, η, of the atom is greater than the surrounding medium causing the refraction shown. The forces F_A and F_B act on the atom, these can be decomposed into the transverse and axial components leading to the forces F_{dip} and F_{scatt} respectively.

We assume the atom has a positive refractive index greater than the surrounding medium, this leads to the refractions as seen in figure 2.6. If the refractive index of the atom was lower than the surrounding medium the dipole force would be reversed and the atom would be repelled from regions of high intensity radiation. This is the case for red-detuned light as would normally be used. The graph in figure 2.6 shows that for red-detuned light the refractive index is positive as described above, however, blue-detuned light gives a negative refractive index.

The dipole force vanishes when the detuning term $\delta = 0$ and hence the applied electric field is resonant. This can be seen in figure 2.6, around resonance absorption maximises and the refractive index goes from positive in the red-detuned regime, crosses reaching zero at resonance and then becomes negative in the blue-detuned region.

To arrive at an expression for the dipole force in which a far-detuned light is used we consider a simple two-level atom and apply an electric field,

$$\boldsymbol{p} = \alpha\boldsymbol{E} \tag{2.46}$$

inducing a dipole moment $\boldsymbol{p}$ for an atom with complex polarisability α which is dependent on the driving frequency ω. The potential describing the atomic

dipole moment and the driving field is[23],

$$U_{dip} = -\frac{1}{2}\langle \boldsymbol{p}\boldsymbol{E}\rangle \tag{2.47}$$

where the angled brackets shown that this term is time averaged for the rapidly oscillating field. Using the definition of field intensity,

$$I = 2\epsilon_o c|\boldsymbol{E}|^2 \tag{2.48}$$

where ϵ_o is the vacuum permittivity. The dipole force can be written as,

$$\boldsymbol{F}_{dip}(\boldsymbol{r}) = -\nabla U_{dip}(\boldsymbol{r}) = \frac{1}{2\epsilon_o c}Re(\alpha)\nabla I(\boldsymbol{r}) \tag{2.49}$$

where we are interested in the real part of the polarisability and not the imaginary part which describes the scattering side of the total interaction, F_{tot}. The polarisability can be expressed by considering the atom in the Lorentz model of a classical oscillator[37],

$$\alpha = 6\pi\epsilon_o c^3 \frac{\Gamma/\omega_o^2}{\omega_o^2 - \omega^2 - i(\omega^3/\omega_o^2)\Gamma} \tag{2.50}$$

where Γ is the excited state decay rate, ω is the driving frequency and ω_o is the resonant transition frequency. For large detunings, to enhance the dipole force and using a beam intensity $I \ll I_{sat}$ we find the dipole potential,

$$U_{dipole}(\boldsymbol{r}) = -\frac{3\pi c^2}{2\omega_o^3}\left(\frac{\Gamma}{\omega_o - \omega} + \frac{\Gamma}{\omega_o + \omega}\right)I(\boldsymbol{r}) \tag{2.51}$$

and the frequency difference is simply the detuning $\delta = \omega_o - \omega$. We can insert this potential into equation 2.49 and using red-detuned light obtain an attractive potential towards highest intensity region of the field. The theory developed in the preceding sections will allow the cooling and trapping of Cs atoms. How this is achieved experimentally will be outlined in the next chapter.

Chapter 3

Experimental set-up

As is the case with cold atom experiments, the work presented here comprises multiple systems all working together seamlessly to meet the conditions necessary to gather our data. This chapter will outline the complex apparatus we use, including, ultra-high vacuum systems (UHV), electronics, frequency stabilised lasers, control sequence systems and carefully controlled magnetic fields. Using these tools we create a cold atomic cloud of caesium and then load them into a microscopic fibre cavity via a dipole trap, producing our atom-photon junction. This atomic cloud is then probed with light fed through the same optical fibre.

This experiment constitutes the ongoing work of multiple generations of students and has evolved over time.The development of this system can be followed in these previous works[38,39,40,41,42]. The current configuration and the data presented in this chapter are due to the huge efforts undertaken by Dr Da Ros[42] who I have assisted. Chapter 4 outlines the recent work and development carried out with the sole intention to improve and carry our main project into the future and is largely the work I have been responsible for. Much of the content in this chapter deals with the experiment in its current configuration in which I have contributed in data collection but not the building of the experiment which, as mentioned previously, can be found in the thesis of successive students. The plans for the future are elaborated on in chapter 5.

3.1   Overview of experiment

Our experiment focuses on an octagonal vacuum chamber containing a small, suspended glass chip. This chip houses our optical fibre which features a laser drilled, transverse, microscopic hole which plays the central role in our set-up. The chip can be seen in figure 3.1(a) with the fibre affixed underneath the chip using vacuum compatible glue. Below the manually drilled macroscopic hole in the chip lies the optical fibre, its microscopic laser-drilled transverse hole lies centrally underneath the chip hole, see figure 3.1(c). This allows unperturbed access for laser light but more importantly it gives us a direct route to transport atoms from our cold caesium ensemble into our fibre hole. This direct transport can be seen in 3.1(b) where the dark red line shows the optical dipole trap confining atoms and pushing them upward from the main body of the caesium cloud. Careful optimisation is required to align the dipole trap and hence the caesium atoms caught within it to the transverse fibre hole allowing light in our fibre to interact at our light-atom junction. Figure 3.1 is extremely helpful to visually understand the terminology used to describe the experiment relating to the chip and the fibre.
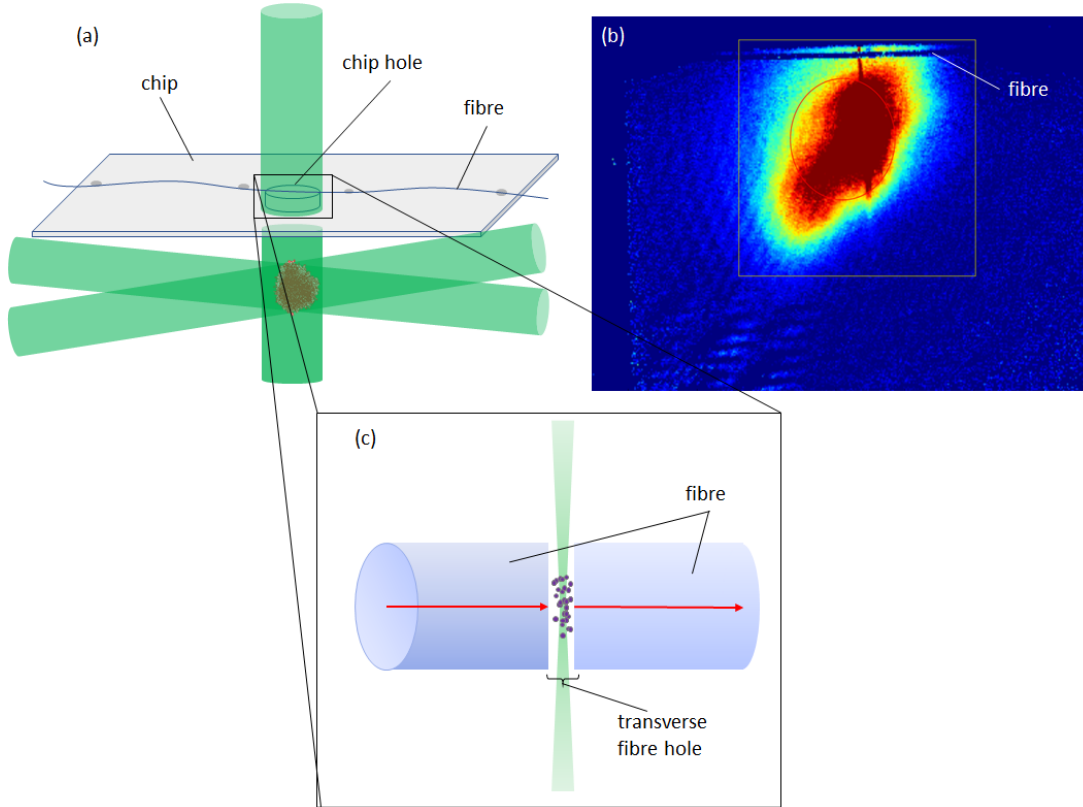
Figure 3.1: Here we see the 3 orthogonal MOT beams pairs trapping a cloud of caesium atoms underneath the fibre-chip assembly (a). (b) shows the dipole trap loading from the MOT, taking the caesium atoms all the way through the fibre hole and then above the fibre exiting the hole (dark red denoting the greatest atom density). (c) shows the propagation of the probe beam (red arrow) through the fibre, passing through the fibre hole and introduced caesium atoms in free space and then re-entering the fibre. The dipole beam with its focused narrow waist coinciding with the fibre hole is represented by the green beam.

3.2   Chamber configuration

To carry out the experimental procedure outlined in section 3.1 requires a finely optimised set-up of various systems working coherently. The first step is to create an environment conducive to creating and maintaining an atomic ensemble at μK temperature. To do this we must create an ultra-high vacuum in our octagonal central chamber to minimise background particle collisions and associated heating. To do this we attach an ion pump to the central chamber via a 6-way cross, this pump maintains our working vacuum pressure of $\sim 1x10^{-9}$ mbar. The introduction of caesium atoms into the chamber is achieved with dispensers positioned on the opposite side of the chamber from the ion pump, see figure 3.2. These dispensers are run at a current of 4.5 A to produce sufficient Cs

atom number. The fibre which contains our atom-light junction enters and exits the chamber through custom made Teflon ferrules, the details of this work can be found elsewhere[41]. The fibre is attached to the underside of the chip using vacuum compatible glue (Dymax Low-Shrink OP-67-LS).
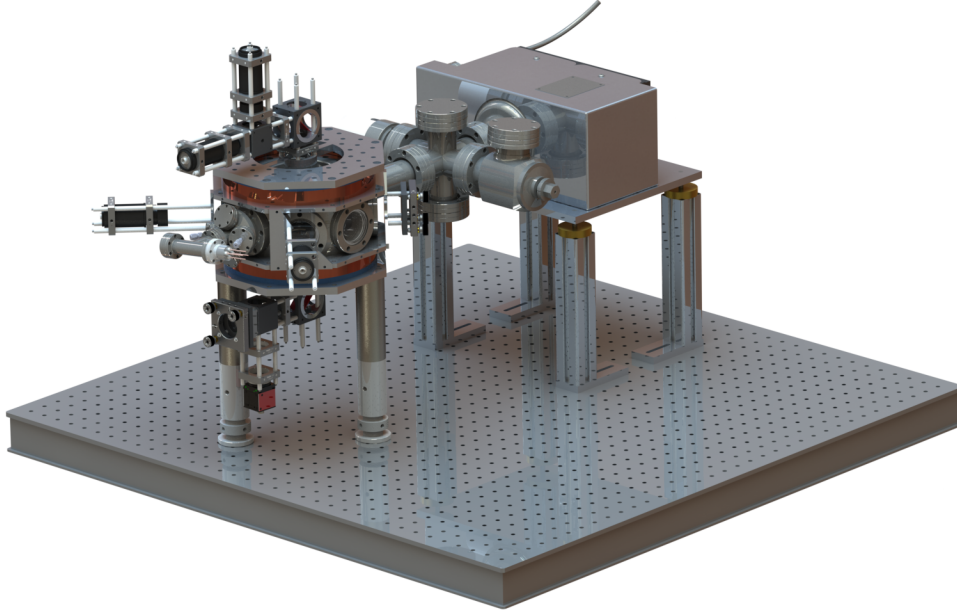
Figure 3.2: A 3D render of the experimental chamber sat atop our optical bench with some optical mounts attached. A six way cross can be seen which is attached to the main chamber and connects it to an ion pump. At the opposite side of the chamber the Cs dispensers can be seen. The magnetic field coils are also visible wrapped around the top and bottom of the chamber as copper wiring.

Outside the camber are an assortment of optics which provide the necessary laser beams and imaging capabilities. The six intersecting beams of the MOT can be seen in figure 3.1 which trap a cloud of caesium atoms below the chip hole and fibre hole. The x-y MOT beam orientations can be seen in more detail in figure 3.3 and the z MOT beams in figure 3.4. In the x-y plane the x and y MOT beams including their counter-propagating retro-reflected counterparts are seen to converge at the centre of the chip. Additionally, it is shown how the horizontal imaging beam is introduced to the x MOT beam path and then how it is redirected to the horizontal imaging guppy CCD using beam splitting cubes. Horizontal imaging is used to monitor the size and shape of the MOT during optimisation.
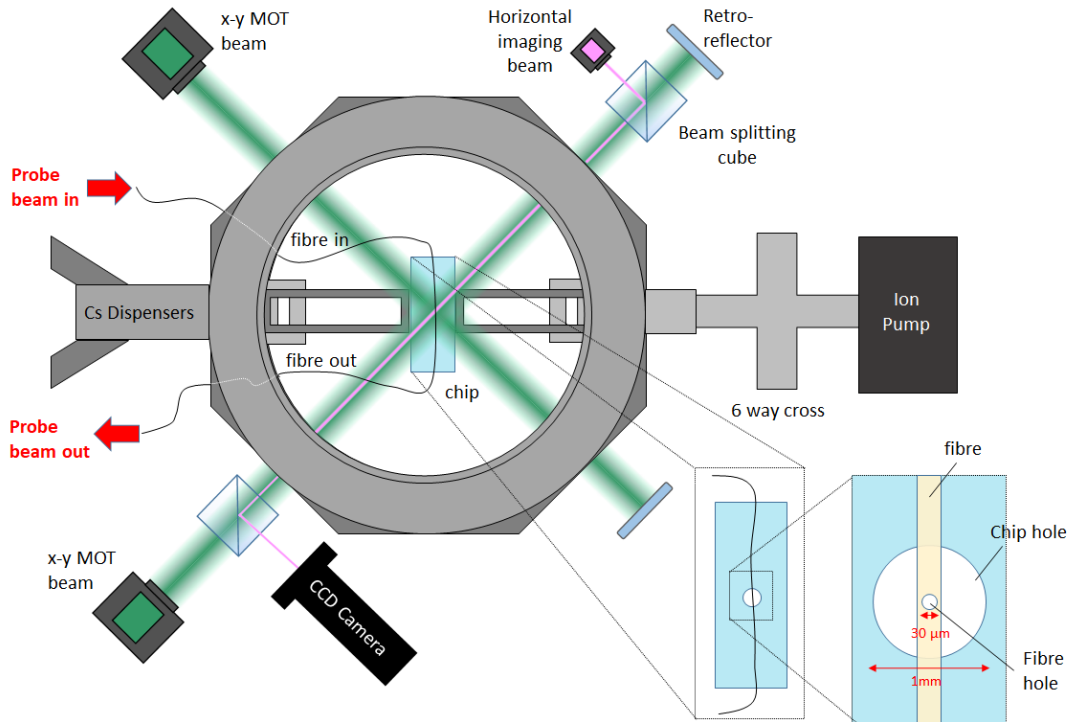
Figure 3.3: Experimental apparatus in the x-y plane. Here we see the chip situated in the centre of the octagonal main chamber. This x-y slice shows the Cs dispensers to the left of the main chamber and the ion pump to the right. A six way cross connects our ion pump and gives us the potential to add more functionality to the experiment at a later date. The x and y MOT beams are shown in green and are retro-reflected to give their counter-propagating counterparts. The pink beam represents the horizontal imaging. Beam-splitting cubes show how this beam is added to the x MOT beam and how it is subsequently removed from the beam path and is directed to the horizontal imaging guppy CCD camera. Lower right inset zooms in on the chip and then the chip hole to highlight clearly the structure of the atom-photon junction. Note that the image is not to scale.

The two vertical MOT beams are independent of one another to give an extra degree of freedom when optimising the MOT position. This is necessary due to the aberrations caused by the glass chip interface interrupting the vertical beam path significantly. If a retro-reflected configuration was used the power of the reflected beam would be reduced and difficult to optimise. The vertical MOT beam paths are shared by the dipole beam which is used to load caesium atom into the fibre hole by pushing atoms up from the MOT. The dipole trap is sharply focused at the chip to create a minimum waist of 13 μm, this is sufficient to thread the atoms into the fibre hole which has a 30 μm diameter and is cylindrical in shape. The tightly focused beam gives a strong radial confinement and a much weaker axial confinement along the beam, leading to the pencil like structure which can be seen in the absorption image, figure 3.1(b). This is ideal for our

needs as it allows us to vertically transport the atoms through the small fibre hole. The vertical beam arrangement can be seen in figure 3.4. The vertical MOT beams, z-up and z-down are introduced at the bottom and top of the chamber through optical cage mounts fitted directly on to the main chamber. Magnetic field coils are also wound around the top and bottom of the main chamber to provide the magnetic fields during an experimental run. Beam splitting cubes mounted above and below the chamber are used to direct the vertical MOT beams into the chamber and mix the dipole trap beam and vertical imaging beam simultaneously. After passing through the chamber a low pass filter is used to prevent the dipole beam reaching the vertical imaging guppy-pro camera. Vertical imaging is important for aligning the MOT underneath the fibre junction and also for aligning the dipole trap with the fibre hole.
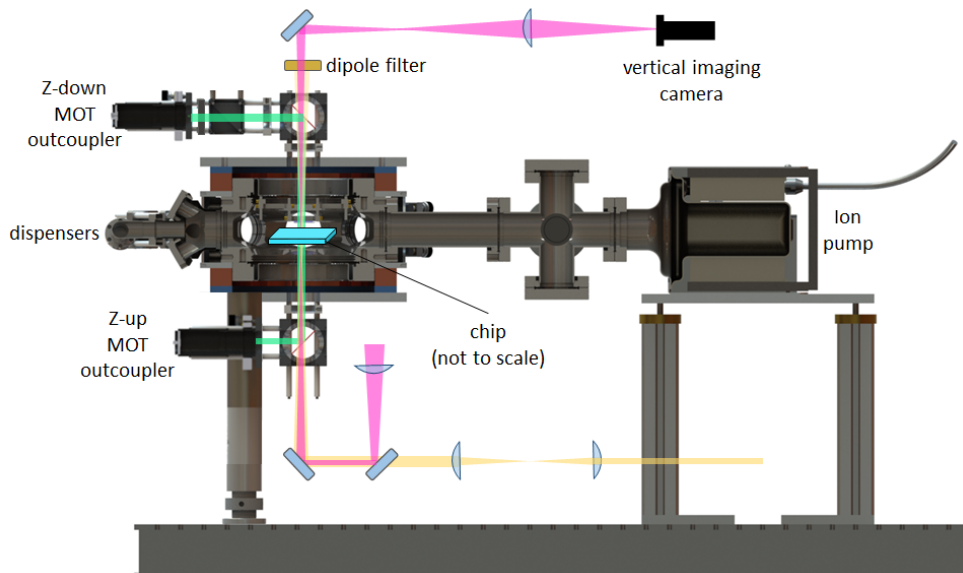
Figure 3.4: Cross-sectional view of the side of the experimental chamber used to house the fibre-chip device including important beam pathways and optics. MOT beams are represented in green, the dipole beam in orange and the vertical imaging beam is pink. A short pass filter is used in the imaging pathway to protect the vertical imaging camera.

The MOT beams and the lasers used for the state preparation of caesium are developed on a separate optical table than the rest of the lasers, the remaining lasers share an optical bench with the experimental chamber. Beams originating from the separate optical table are transferred to the bench housing the experiment via polarisation maintaining optical fibres. The probe beam used for interacting with the atoms in the fibre junction is produced by a laser on the optical table with the main chamber along with the new-ref laser which is used to lock the

probe. A detailed list of all the lasers used in this experiment can be found in table 3.1.

3.3   Laser systems

Precise control of multiple lasers and their respective frequencies and powers allows for remarkable control of the external and internal states of atoms. Sections 2.1.2 and 2.2 set out how we use lasers to manipulate the position and temperature of atoms as well as how we can exploit their internal energy structure. Here we detail the lasers which enable us to carry out these techniques.

Our experiment utilises several external cavity diode lasers or ECDLs, which are all home-built, a single Toptica TA pro and a Nufern fibre amplifier which is seeded by a single mode Mephisto. All of these lasers and their associated applications are laid out in table 3.1.

Laser	Application
Toptica TA Pro	Responsible for all laser cooling x, y and z MOT beams
Nufern	Provides the vertical dipole beam used to load caesium atoms
Reference	Spectroscopy used for locking of cooling beams and vertical imaging
Repumper	Provides repumper light for MOT setup and M_F optical pumping
Fibre Probe	Probe light for measuring caesium absorption, also used for horizontal imaging
New Ref	Spectroscopy used for locking of probe beam, EIT control beam and F optical pumping
EIT Signal	EIT signal beam

Table 3.1: A list of the lasers used and the role each plays within the experiment.

Apart from the dipole beam which has a wavelength of 1064nm (which is far red-detuned from the optical caesium transitions to magnify the dipole force and minimise heating and scattering) precise control of each laser's frequency is essential for manipulating atoms to the extent we require. This is accomplished in two ways in our set-up. The first is by piezoelectric crystals mounted to a diffraction grating which can tune the laser frequency very precisely. This is done in an ECDL configuration as the laser diodes alone would give line-widths of 100GHz, which is not narrow enough to elicit electron transitions in the hyperfine region as we require. Additional frequency control is given through acousto-optic modulators or AOMs, these devices allow very fine changes in laser frequency and can be controlled remotely in-sequence throughout different stages of the experiment. These fine-tunings are indicated by some of the small arrows seen in figure 3.5.

Other arrows indicate off-set locking which is a technique that has been employed in this experiment since its inception and has been explained thoroughly in these other works[39,40]. This technique is predicated on practice called saturated absorption spectroscopy, a full explanation can be found in elsewhere[38,39,40].

I will give a brief outline of absorption spectroscopy here to provide a preliminary overview of the laser system. Using a room temperature vapour cell containing a specimen such as caesium we can apply a strong pump beam and a weaker counter-propagating probe beam. Only those atoms moving perpendicularly to the radiation of both fields will be on resonance (for a particular atomic transition). The strong pump beam will depopulate the ground states leading to the counter-propagating probe beam being transmitted, thus producing the characteristic saturated absorption spectroscopy signal. Furthermore, at the instance where atoms are moving such that the probe laser falls directly between two energy levels a phenomena known as a crossover peak can be seen in the spectroscopy. This detailed spectrographic signature can then be used as a reference with which other lasers can be locked. The adjustments to laser frequency of this nature can span a large range of 150 MHz.
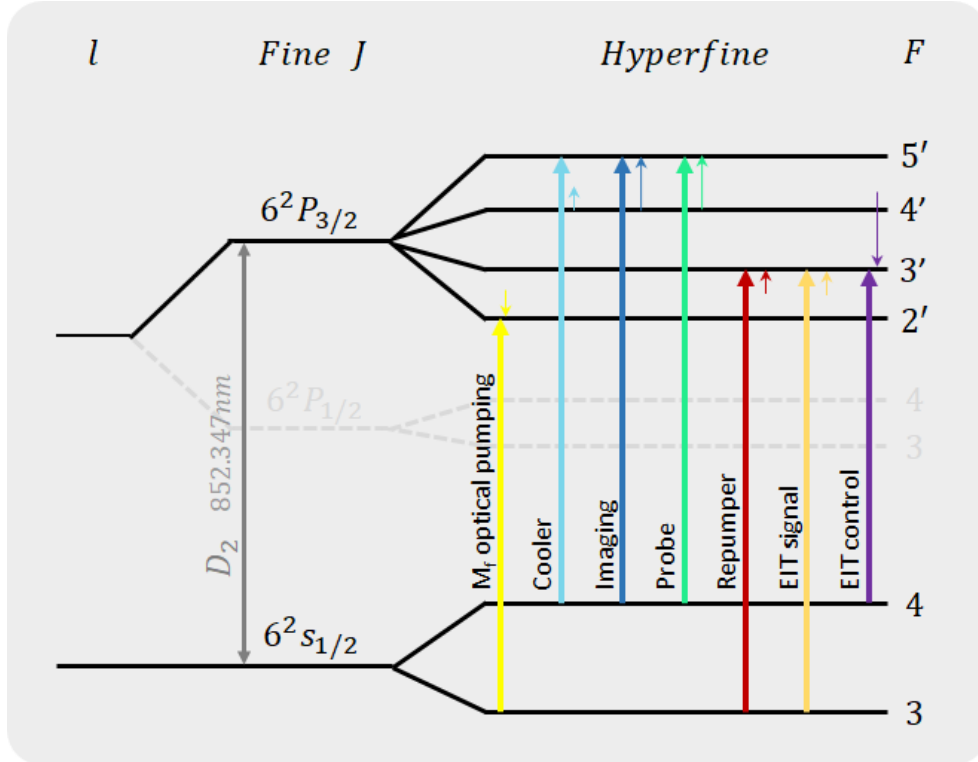
Figure 3.5: Caesium atomic level structure populated by various arrows representing the multiple lasers used in this experiment. This diagram shows which lasers are resonant with their specific electron transition. Small arrows represent the detunings that are instituted through various means in the experimental set-up.

The D_2 line transition of caesium requires that we used light of near resonant 852 nm wavelength which can then be tuned using AOMs and diffraction gratings. The cooling, imaging and probe light takes advantage of the hyperfine structure of caesium using the $6^2S_{1/2}, F = 4 \rightarrow 6^2P_{3/2}$, F = 5'. Here prime represents a state is in the excited manifold, $|1\rangle$. To provide cooling the MOT beams require closed transitions such that the cycle of absorption and emission between two states can be perpetual. The $F = 5'$ state has a small chance of decaying into the $F = 3$ via a magnetic quadrupole transition. This can be mitigated by introducing a repumper beam which can be seen in figure 3.5 represented by the red arrow. This excitation pathway reintroduces electrons into the cooling cycles by pumping them out of the $F = 3$ state and into the $F = 3'$ state.

The M_f optical pumping beam is used to pump atoms into an absolute ground state of $6^2S_{1/2}, F = 3, M_f = 3$. The EIT signal and control beam will be outlined in section 4.3.1. Below an optical schematic is included for the production of the MOT beams and vertical imaging in our experiment, see figure 3.6. This shows

the setup for the separate optical bench which is isolated from the bench housing the experimental chamber. Beams are transferred from this optical bench to the experiment through polarisation maintaining optical patch cables.
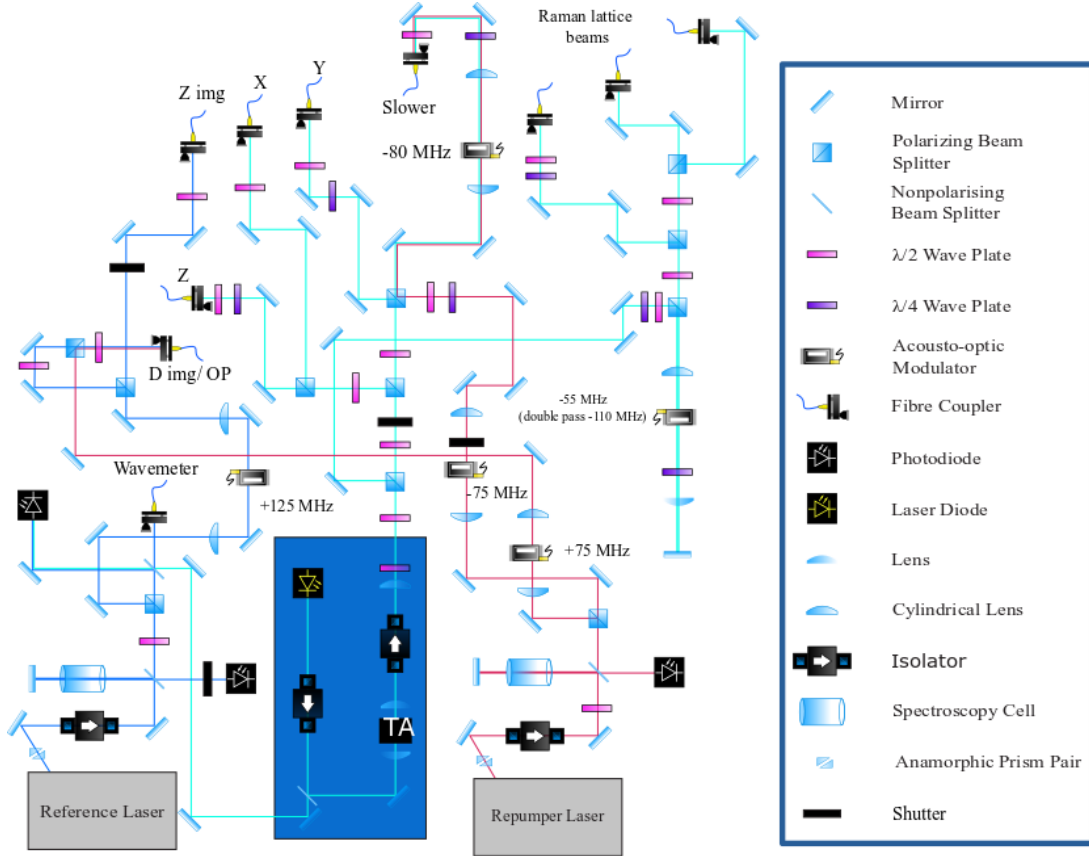
Figure 3.6: Optical set-up for the caesium MOT and vertical imaging

3.4 Magnetic fields

Magnetic fields play a vital part in the experimental procedure. Zeeman splitting is generated in the caesium atoms by our MOT coils. This allows us to produce the magneto-optical trap of caesium at the centre of the experimental chamber. These copper coils can be seen at the top and bottom of the 3D render of the vacuum chamber, see figure 3.2. On top of these coils, three sets of compensation coils are also acting on the system. One for each axis, x, y and z. In this experiment the z compensation coil is an important parameter to fine tune as this offsets the magnetic field in the chamber vertically and is used to push atoms upwards towards the fibre interface helping to load caesium atoms into the fibre hole.

Characterisation of the MOT coils

During the lifetime of this experiment characterisation of the MOT coils within the chamber has not been possible as this would require disassembly of the experiment. Fortunately, one of the improvements to the system was the rotation of the chamber by 90° and the insertion of a new chip. This will also rotate the chip by 90° and will enable the dipole trap to be oriented horizontally. Hence, the Trapped atoms will be to the side of the chip and the dipole trap will load from the side horizontally into the fibre hole. This mitigates the effect of gravity acting directly against our atom migration into the fibre hole and additionally the radial confinement of the dipole trap will be acting against gravity rather than the vertical which is greater leading to better confinement. This will reduce the heating caused by the dipole trap acting vertically to load atoms into the fibre hole as is the case in the set-up before the chamber rotation. More details of this can be found in chapter 5. This interruption in data gathering presented the opportunity to remove the MOT coils from the chamber and characterise the magnetic field strength within the chamber. For logistical reasons this was not carried out at the outset of the building of this experiment and due to the ability to produce a reliable MOT was not regarded as a priority. As the disassembly of the experiment provided the opportunity to carry out the analysis it was taken. We compare simulations of the magnetic field against direct measurements to better understand the behaviour of our system and to provide insight for future upgrades.

With the MOT coils unmounted from the chamber it was possible to insert a gaussmeter at the centre of the coils and hence characterise the magnetic field the MOT coil produces during experimental runs in an anti-Helmholtz configuration. Figure 3.7 shows the magnetic field strength as a function of distance both radially and axially. Figures A and B show the variation in magnetic field strength radially from the centre of the coils (at 0 cm) and moving outwards radially towards the coils themselves. The coloured lines represent the magnetic field strength due to a different applied currents. C and D show the magnetic field strength variation by axial distance. At 0 cm the gaussmeter is central between the two coils, increasing position moves the sensor axially in the z direction but

maintaining a constant radial displacement away from the circular coil pair. Note that the centre of the coil is not a zero field strength due to the outer offset coils usually present in the main experiment that are configured in the Helmholtz configuration which would cancel to form a zero field at the center of the coil pair, however, with the MOT coils removed from the main experiment they are not benefiting from the superposition of the offset coils.
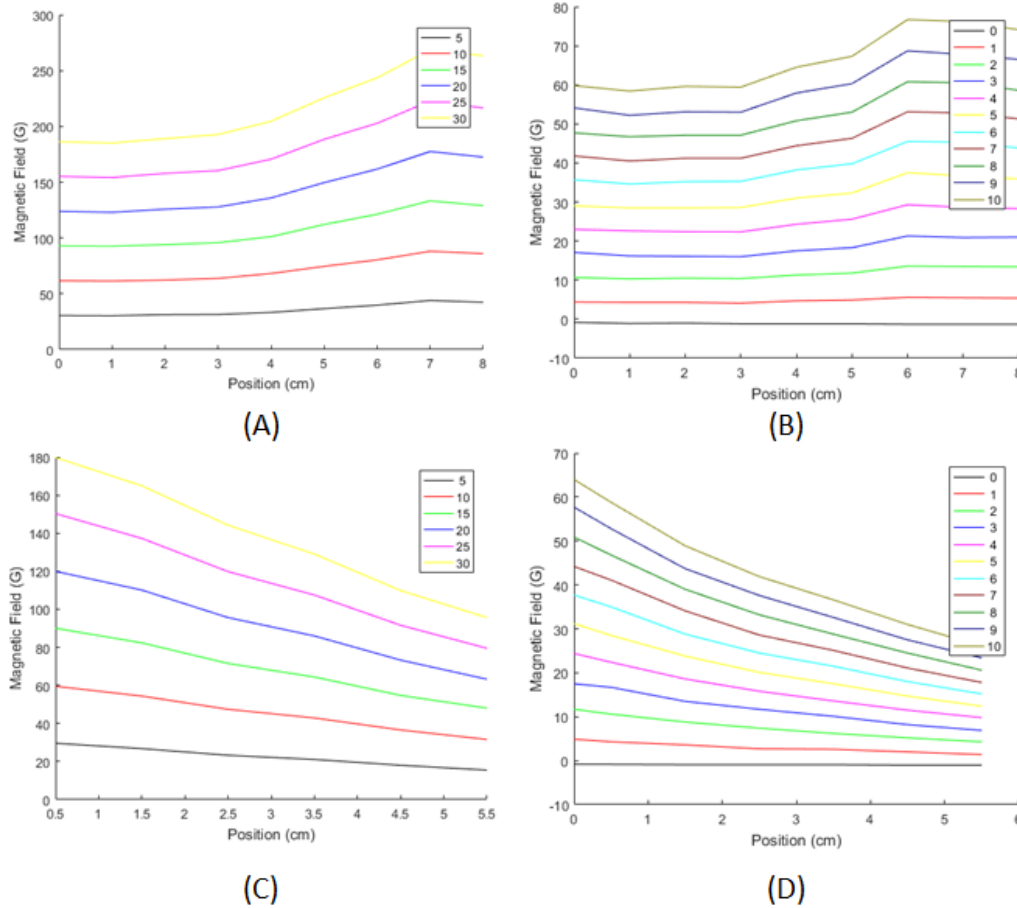
Figure 3.7: Characterisation of the MOT coils attached to experimental chamber. Magnetic field strength measured via gaussmeter. A and B show the variation in magnetic field strength with radial distance from the approximate centre of the coils (the sensor begins in the centre of the coil and moves radially outward toward the coil itself). A shows the relationship in coarse jumps of current (the legend signifies the coil current via colour in Amps) whereas B gives finer increments of current. C and D show the variation in magnetic field strength with axial distance from the approximate centre of the coils (the sensor is placed in the centre of the coil and moved axially away from the coil towards the centre of the coil pair). Once again with C being coarse jumps in current and D fine.
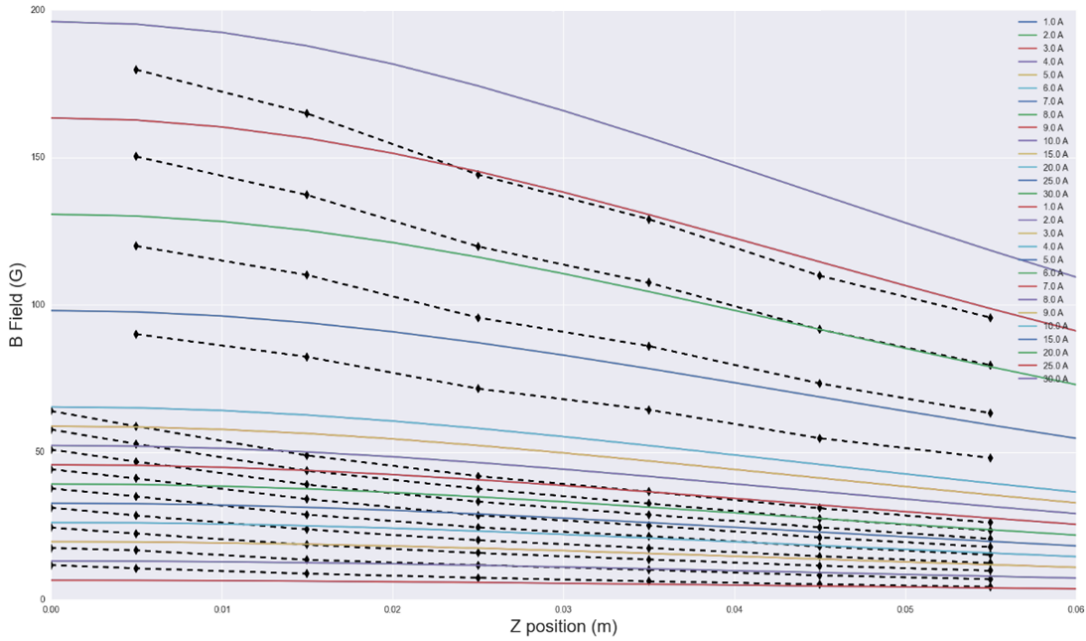
Figure 3.8: Axial field data for the MOT coils plotted with simulation data (dashed lines). It is apparent that the simulated magnetic fields which have previously been calculated do not correlate perfectly with our measurements. However, the overall shape of the relationship is still similar. Discrepancies between simulation and data appear to be greater at higher current values and greater distance from the centre of the chamber. This will be useful when optimising the experiment in the future.

It can be seen in figure 3.8 that the measured magnetic field matches the shape of the simulated field but has large differences in field strength and the discrepancies grow at greater currents and distances from the chamber coil centre. This is promising as the field strength is most important at the centre of the chamber where the chip is located. Additionally, such high field strengths are not applicable to our current system, however it may become applicable in future iterations of the experiment. These results will therefore need to be taken into account when data collection is resumed.

3.5 Imaging

Throughout this experiment both the imaging and probing of an atomic cloud is carried out using absorptive processes. These techniques rely on the absorptive property of atoms which are illuminated with resonant light. We use absorption imaging to visualise the atomic cloud, this allows us to optimise its position, shape, atom number and density, reaching a satisfactory condition for analysis. Once this has been obtained atoms can be loaded into the fibre interface where

absorption measurements can be taken to characterise the interface's atom-photon coupling strength. This interface will be outlined in section 3.6.

The measurement of cold atoms is no simple task as a direct measurement of the atomic cloud is impossible. The most common method used in cold atoms experiments is absorption imaging. This method is destructive in the sense that it leads to state changes and heating of atoms but due to its reliability and it being relatively easy to implement it remains a mainstay of the field. Non-destructive methods such as fluorescence imaging are also used in this experiment, this helps characterise MOT loading in real time but is limited to this role.

To image an atomic cloud a resonant probe beam is directed toward it. Along this incident beam path a CCD camera is used, this can record the intensity distribution of light spatially[43]. An atomic cloud will absorb photons from the resonant probe beam reducing the intensity of the beam measured at the CCD, effectively casting a shadow. To create an image from this a sequence of 3 images are taken in quick succession. An image is taken of the probe beam with no atoms obstructing the beam, then an image is taken with the beam applied with an atomic cloud in the beam path. The intensity ratio is taken. Then a single image records the intensity of light with no beam and hence measures the background radiation of the experiment which is subtracted from our intensity ratio. This gives us our absorption image that shows us the shape and size of the atom cloud. This process is depicted in figure 3.9 which depicts each image described previously.
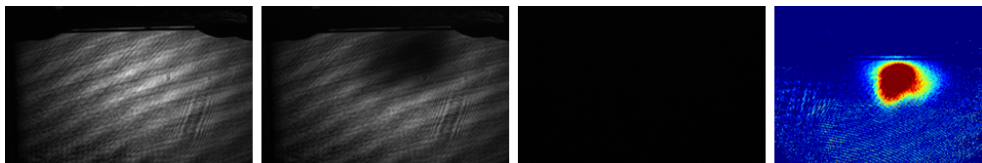
Figure 3.9: The first image depicts the probe beam incident on the CCD with no atoms, the second shows the laser applied to a cloud of atoms and the third image shows the background radiation. The final image shows the false colour absorption image of our Caesium MOT underneath the optical fibre.

The attenuation of the laser due to the atom cloud can be quantified using the Beer-Lambert law[23],

$$I(x,z) = I_o(x,z)e^{-n(x,z)\sigma} \tag{3.1}$$

where $I(x,z)$ gives the intensity of the beam reaching the CCD at a particuar position in the x-z plane and I_o is the initial beam intensity before hitting the cloud. The absorption cross section is defined as,

$$\sigma = \frac{3\lambda^2}{2\pi} \tag{3.2}$$

and the column density of the of the sample at the same position in the x-z plane is given by,

$$n_y(x,z) = \int n(x,y,z)dy \tag{3.3}$$

The ratio, I/I_o is calculated by our absorption imaging technique. We can then rewrite the equation for the intensity such that,

$$n_y = -\frac{1}{\sigma}ln\left(\frac{I}{I_o}\right) \tag{3.4}$$

At atomic resonance and a regime where the probe beam is much weaker than saturation ($I_o \ll I_{sat}$), we can then integrate over the column density for each pixel. Both an atomic density and total atom number can then be calculated to characterise our atomic cloud.

3.6   Atom detection at the fibre void

The main goal of this experiment is to detect atoms within the fibre void and maximise the interaction of the probe light coupled to the fibre with these atoms. Much like the previous chapter, this is quantified by measuring the absorption of the probe light after it has crossed the fibre hole, passed through the atom cloud (having been attenuated) and then re-enters the fibre. This fibre then exits the vacuum chamber and is directed toward a single photon counting module (SPCM). By comparing the photon count which occurs when the caesium atoms are present to the situation when they are absent, we obtain a quantitative measure of the atom cloud absorption of the resonant probe beam. This method also allows us to factor in the light lost due to the fibre hole itself and the non-zero loses as the probe light is coupled back into the fibre on the far side of the hole. The transition used for this absorption measurement is $6^2S_1/2, F = 4 \rightarrow 6^2P_3/2$, F=5', this can be seen plotted on figure 3.5. An SPCM is necessary due to the low photon count required to keep the probe intensity below saturation and

hence allow us to measure the absorption instead of fully saturating the cloud. To ensure the atoms counted are a result of the probe beam great efforts are taken to shield the module from background radiation. On top of this a background radiation of each experimental run is taken when the probe beam is disabled, this can then be subtracted from the photon count. The final step taken to eliminate background noise from our data is to repeat the experimental run many times and taking the mean photon count. In this way the effect of shot noise on our data can be minimised.

The fibre hole itself is a 30μm diameter, cylindrical, transverse hole which reaches through the entire width of the fibre. The fibre is a 780 HP single mode optical fibre from Thorlabs. The hole is orientated orthogonal to the axial axis of the fibre. For light to pass through the fibre it must leave the exit facet of the fibre hole, traverse the 30μm free space expanse and then re-enter the fibre at the entrance facet. The hole was created through a laser drilling process and the work was carried out by Workshop of Photonics (WOP). The work done to improve this aspect of the system, specifically the transmission efficiency of the fibre hole itself to the probe light can be found in section 4.1.1. For the experiment as it stands the transmission efficiency of the fibre hole is 20% at a wavelength of 852nm, this figure includes the coupling losses into the fibre.
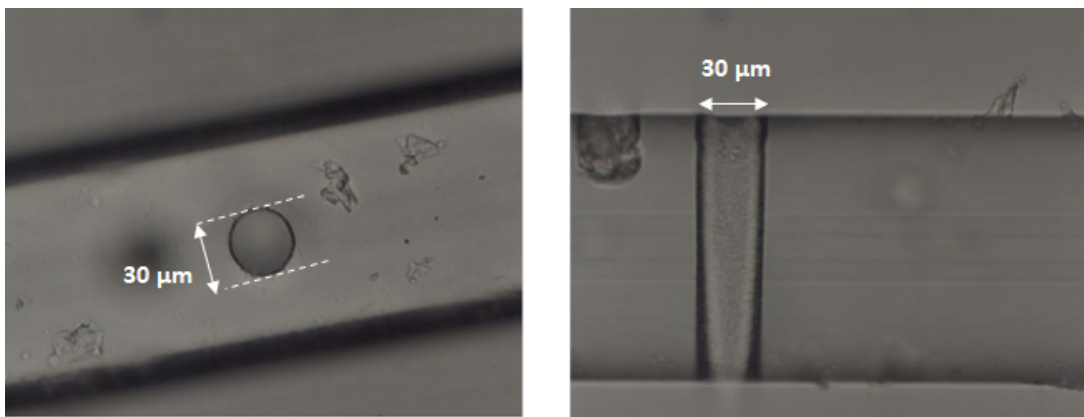
Figure 3.10: A top-down (left) and side-view (right) of the optical fibre with a transverse cylindrical hole. Images provided by our fibre hole manufacturers WOP (Workshop of Photonics).

3.7 Control software

The experiment is run using a control system operated through a National Instruments PXIe-8130. It uses both analogue and digital output cards for signal generation. The software used to run the control system uses the Pyplayer framework and was created by M. Jones and A. Paris-Mandoki[38,40]. The control sequence allows us to change parameters between experimental runs and within a series of experimental runs while changing a parameter systematically. Using this in conjunction with real time absorption imaging provides a powerful tool to optimise the experiment.

Control of the entire experimental setup is performed remotely through channels which can operate a specific function when a voltage signal is applied. Multiple shutters are driven by this mechanism which allows lasers to be blocked and unblocked rapidly. Additionally, AOMs and locking mechanisms can be altered remotely providing real time manipulation of laser frequency. Magnetic fields can also be ramped and switched on and off during an experimental sequence.

3.8 Results

Similarly to the absorption imaging of the last section the absorption of the probe beam by the atom cloud can be quantified using the Beer-Lambert law. Equation 3.5 can be shown to be related to optical depth (OD) where $OD = n_y \sigma_o$,

$$n_y(x,z) = -\frac{1}{\sigma_o} ln\left(\frac{I_{out}}{I_o}\right) = \frac{OD}{\sigma_o} \tag{3.5}$$

The absorption can then be defined as

$$Absorption = (1 - e^{-OD}) \tag{3.6}$$

With the dipole trap successfully loading atoms into the fibre hole we can then measure the absorbance of our cold atom cloud. We couple a weak probe beam (making sure not to saturate the caesium atoms in the dipole trap) into the bare fibre this then guides the light into the atom cloud at the fibre void. After passing through the caesium cloud, light is then re-coupled into the fibre, we direct this attenuated light onto the SPCM for measuring. The number of photons striking the SPCM is then recorded via high frequency binary counter chips which are

interfaced with using an Arduino Uno.

The highest absorption so far measured was $87 \pm 2\%$ which is the equivalent of an optical density of $2.1 \pm 0.2\%$ when equation 3.6 is applied. As this topic was undertaken by Dr DA Ros and I only assisted, the full details of these results can be seen in full in Dr Da Ros's thesis[42].

Chapter 4

Development of experimental system

This chapter presents all of the work undertaken to improve the system and carry the experiment forward. Firstly, I will present the work on the replacement of the main experiment's optical fibre. We investigate the effects of variously shaped laser machined transverse holes, including their transmission and chip hole oscillation stability. These experiments will include measurements taken to determine the optimum set-up for a future EIT (electromagnetically induced transparency) experiment in the main chamber. Carrying on from this, the basic theory of EIT will be introduced, along with the caesium vapour cell tests that were carried out to display this behaviour. Finally, initial analysis on an integrated waveguide chip provided by FBH (Ferdinand-Braun-Institut) on behalf of the ErBeStA consortium will be presented.

4.1 Fibre analysis

This first section details a substantial amount of work that has been carried out towards improving the atom-photon junction of the experiment. This includes work on the shape of the laser-drilled hole in the fibre and importantly, how this effects the efficiency of light transmission and also how this effects the polarisation stability of the light of the fibre as it transverses the fibre hole. The size of the larger chip hole is also investigated with regard to the structural stability of the chip-fibre assembly - see figure 3.3 for a reminder of the chip hole and fibre hole spatial arrangements. This section will combine the motivation for the work

carried out and the methodology used to implement it. Any results gathered will be discussed along with their significance towards improving the experimental system.

4.1.1   Drilled fibre testing

A major limiting factor in the caesium atom-photon coupling experiment is the significant losses in probe beam intensity throughout the system. A significant source of these losses occur at the transverse fibre hole. The current set-up employs a circularly drilled hole which is not the best shape to create the maximum overlap between the fibre waveguide mode and the transmitted light through the void, according to theory. An optimised shape of the drilled hole can drastically reduce the photon losses at the hole. Work has been carried out from within our group to simulate the optimum hole shape for light transmission[44]. A key motivation towards reduced hole losses comes from the interest in utilising holes within optical cavities or resonators which can include cold atoms and hopefully reach the strong coupling regime. By decreasing losses at the hole we should increase the Q-factor of any resonator or optical cavity system that can be created using, for example, Bragg gratings[45,46] (section 5.3 shows one of our chips with a ring resonator design, which could be integrated with a hole in future iterations).
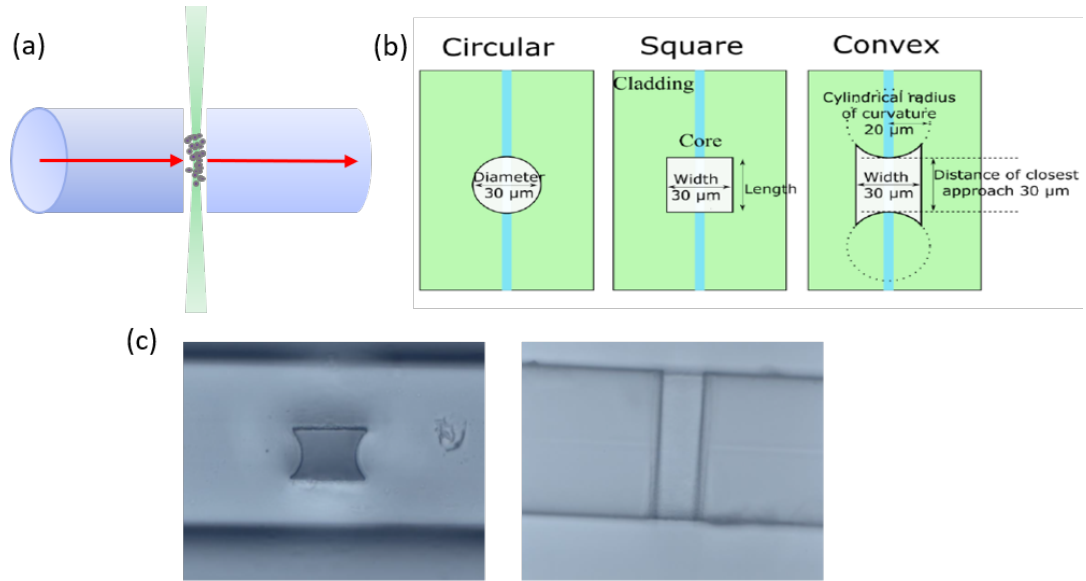
Figure 4.1: In (a) we see the probe beam (red arrow) travelling through our bare fibre and then traversing the gap containing cold caesium atoms trapped by a vertical dipole beam (green) at its focus. Schematics showing the top-down views of the three laser drilled hole shapes (b), the blue channel is the fibre core and the pale green is the fibre cladding. Microscope images (c), showing a convex hole drilled into a fibre from the bottom (c, left) and from the side (c, right). Hole images courtesy of Workshop of Photonics (WOP).

To achieve greater light transmissions 18 new bare fibres of both single and multi-mode with laser drilled holes of various shapes were prepared for us by Workshop of Photonics (WOP). Table 4.1 lists all of the fibres which survived laser drilling and transportation. Each of these fibres were then characterised to allow comparison between the theoretical transmission values as set out by Cooper et al.[44], and secondly to provide a candidate for replacement of the fibre currently installed in the atom-photon interface experiment. A table of these fibres and their associated properties can be found below, see table 4.1. A large variety of fibres were manufactured, with combinations of hole shape, fibre type, chip hole size and even fibre length. Unfortunately due to the fragile nature of fibre-chip arrangement some fibres were broken completely, additionally the drilling process itself is not perfect as we do see certain chips with very low coupling such as chip 16, showing that some defect is severely hampering it. Fibres could also be seen to display bright spots along themselves showing that containment of the light inside the core was failing and likely leading to large losses in transmission at these zones.

To test the fibres a standard optical system for fibre coupling of laser light was

assembled. Light was first fed into a polarisation maintaining 780 HP patch cable from a 780 nm Toptica TA laser. The probe light which will be used in the main experiment is 852 nm however 780 nm light lies within the fibre specification and the practicalities of the laboratory environment made it impractical to carry out the experiment with 852 nm light. Each of the fibres required connectorisation with a spring clamped Thorlabs BFT1 connector after they were first stripped of their outer cladding and cleaned. As both ends of each fibre are fixed to a glass chip with only vacuum compatible glue and with the sensitive laser drilled hole located at the centre of the chip this process is extremely delicate and painstaking. Multiple fibres were damaged beyond use both in transport and during analysis. In addition to these steps, each fibre end-facet required rigorous cleaning and polishing to ensure the greatest possible beam transmission so as to give the best possible transmission for each hole type. Substantial losses due to poor fibre polishing would hinder any comparison between the various hole shapes and the theoretical values. Once maximum coupling was thought to have been achieved by use of a photo-diode, the outcoupled beam power was then measured using a power meter, this was repeated multiple times and was optimised after each connector reinsertion to establish reliable measurements.

The transmission column in table 4.1 gives the transmission as a percentage of the total power just before entering the incoupler at the bare fibre connector. The corrected transmission column corrects this raw value using a maximum transmission value measured for each fibre type without a fibre drilled hole. We will concentrate on the raw data as corrected values give misleading numbers, which cannot be physically possible as we see greater than 100% transmission. This is due to the maximum transmission values measured not being at the true maximum during free-space incoupling to the fibre, it is likely a local maximum was measured or inadequate fibre end polishing caused this. In this situation a local maximum in coupling is when mirrors are adjusted along the beam path to maximise transmission, however, if the beam is clipping the incoupler or the has a non zero order mode this maximum may not be the absolute but rather a local maximum.

Fibre Model	Chip Number	Transmission (%)	Transmission corrected (%)	Hole shape	Hole size (um)	Chip hole diameter (mm)
Single mode PM 780 HP	1	N/A	N/A	Circular	30	1
	2	10.7	13.2	Square	30	10
Single mode 780 HP	3	24.3	31.6	Square	30	16
	4	28.7	37.3	Convex	30	16
Multimode FG010LDA	5	N/A	N/A	Circular	30	10
	6	24.6	51.2	Square	30	10
	7	17.2	35.9	Convex	30	10
Multimode FG025LJA	8	10.7	N/A	Square	30x20	2
	9	7.7	N/A	Square	30	1
	10	11.6	N/A	Convex	30	1
Multimode FG105LVA	11	46.9	81.6	Circular	30	2
	12	57.1	99.4	Square	30	10
	13	64.4	112.0	Convex	30	2
Singlemode SM800-5.6-125	14	24.0	32.8	Square	30	1
	15	22.1	30.1	Square	30x20	10
	16	0.5	0.7	Convex	30	1

Table 4.1: Drilled fibre details

The tabulated fibre results can be seen plotted in figure 4.2. Due to the variability in the chip designs and the random structural failure of multiple chips it is difficult to make a definite statement about the agreement with theory. We do see much higher transmissions with multi-mode fibres but this is to be expected, and for our purposes multi-mode fibres will not be the best candidates for inserting into our experimental chamber. We do see in general that convex holes tend to outperform square holes and then the same can be said for square holes giving better transmissions than circular holes. This is in agreement with the theoretical predictions that convex > square > circular in terms of maximum transmission[44]. This is most clearly seen in the FG105LVA fibre series. From these fibres the best candidates for insertion into our experiment are chip 3 and 4. However, after taking measurements chip 3 suffered severe damage leaving chip 4 as our most promising candidate.
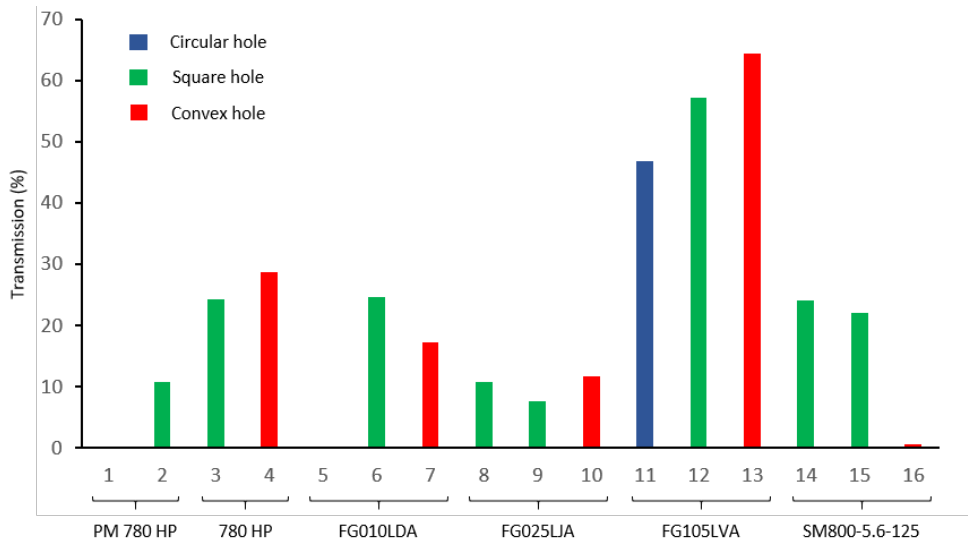
Figure 4.2: Graph displaying the non-corrected fibre transmission values for all of the hole-drilled fibres.

4.1.2 Oscillation testing

Fibre hole transmission is only one aspect of the fibre that must be considered as we prepare to replace the current fibre in our vacuum chamber. Another important consideration can be seen when we observe the chip-fibre structure, see figure 3.1(a). The transverse laser drilled hole of the fibre is situated in the centre of a circular hole which has been manually drilled into a glass chip to act as a housing structure for the experiment (this is important to allow unimpeded

transferal of caesium atoms from the MOT into the fibre void via the dipole trap as seen in figure 3.1). It is this chip hole which is the next aspect we investigated to choose the correct fibre candidate to insert into our experiment.

The current fibre is fixed taut to the chip using a vacuum compatible, UV-cure glue (Dymax Low-Shrink OP-67-LS) and hangs freely under its own weight over a 1 mm diameter expanse. This distance was sufficient to allow free passage of dipole and MOT beams through the chip. However, experience has shown that the rough surface of this manually drilled hole in the glass plate disrupts our MOT as it is pushed towards the fibre via magnetic offset fields, and hence, reduces caesium loading into the dipole trap. A simple solution to this problem is to increase the diameter of the hole thereby reducing MOT beam aberrations. The fibre-chip combinations tested vary in chip hole diameter from 1-16mm as seen in table 4.1. The longer free-hanging length of the fibre in these chips brings into question the mechanical stability of the fibre. Oscillation of the fibre - much like a guitar string over its sound hole - would be extremely detrimental to dipole loading and therefore any atom-light interfacing experiments in the future. Oscillations at a maximum of half the fibre hole diameter would be a minimum requirement for the set-up to be feasible, $z \ll \frac{d}{2}$. Movement large enough to bring the fibre hole edge in contact with the dipole trapped atoms would lead to considerable thermalisation of the confined atoms.This is due to fibre and experimental being at an ambient room temperature which is orders of magnitude higher than the μK kelvin temperature of the confined atoms leading to the loss of trapped atoms.
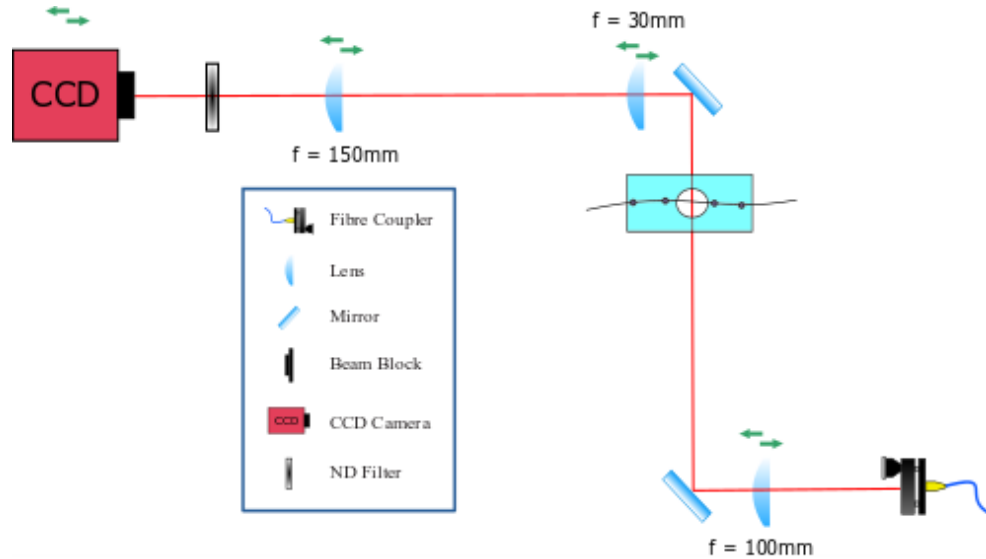
Figure 4.3: Optical diagram of the set-up used in the fibre oscillation measurement experiment on the mock-chip. Green arrows represent lenses that were mounted to have tuneable positions to optimise imaging.

To measure the oscillations of the fibre an imaging system was assembled as seen in figure 4.3. An outcoupler provides a convenient source of 780 nm wavelength laser light (where the source of the light is a Toptica Tapered amplifier coupled into a fibre), which is then immediately collimated into a 15 mm diameter beam for imaging of the fibre. This light then passes through our mock-chip which is identical to our laser drilled fibre-chips apart from the transverse cavity. This was done as the laser drilled holes are prohibitively expensive and delicate for prolonged handling. After passing through the chip the light is then focused onto a CCD Guppy camera (F-038) using a telescope consisting of a 30 mm and 150mm focus lens producing a magnification factor of x5. To obtain a calibration measurement a USAF 1951 target plate was first placed at the focal point of the telescope giving a resolution of ~ 4 μm/pixel. Images taken of the fibre with a known diameter of 245$\pm$15 μm agreed well with the test target plate resolution.

In order to capture both high and low frequency oscillation sources, images needed to be taken at both short and long-time scales. This was accomplished by configuring an Arduino Uno to send a trigger pulse in a logarithmic fashion, spanning time intervals from 100μs to 100000s. Such a large timescale on the upper end of the range is probably not relevant to our experiment but was no more difficult to run and was interesting to capture longer time scale effects for curiosity's sake. Matlab was used to interface with the guppy camera and store

the images.   Figure 4.4 shows the analysis performed on the images whereby
an edge recognition function was used in Python to find the relative motion of
identifiable features along the cross section of the fibre.   Figure 4.5 shows that
the oscillation of these recognisable features deviate from stationary by no more
than a single pixel. This shows that the fibre is remarkably stable under regular
lab conditions (using vibrationally isolated optical benches) and undergoes a
maximum displacement of around 4 μm, assuming the small oscillations seen are
not simply artefacts of the image analysis performed.
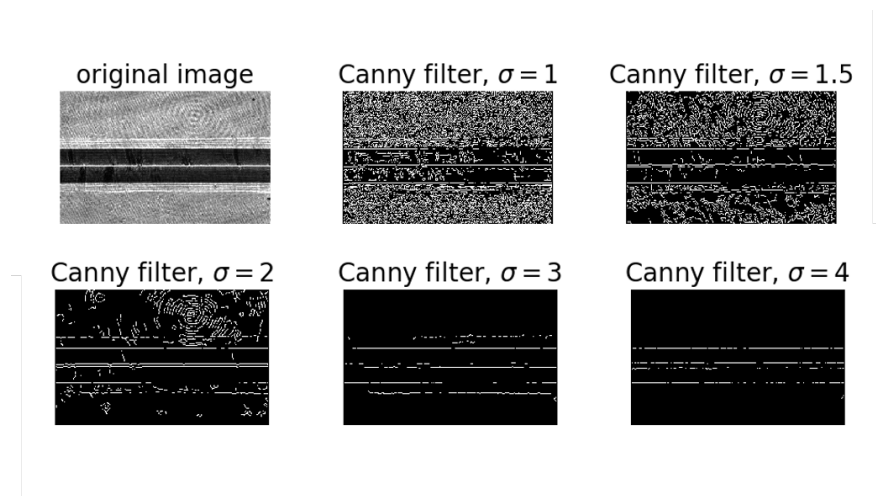
Figure 4.4:   Examples of images taken edge-on during the time lapse (top left).   The
bright central region is the core of the fibre and was most sharply in focus, the darker
region immediately above and below is the surrounding cladding.   The grey outer region is
simply empty space displaying interference effects. The canny filter recognises edge structures,
increasing the σ value reduces noise allowing the edges to be more easily selected. However
this leads to data gaps with require smoothing and hence increases the error in the fibre
displacement.
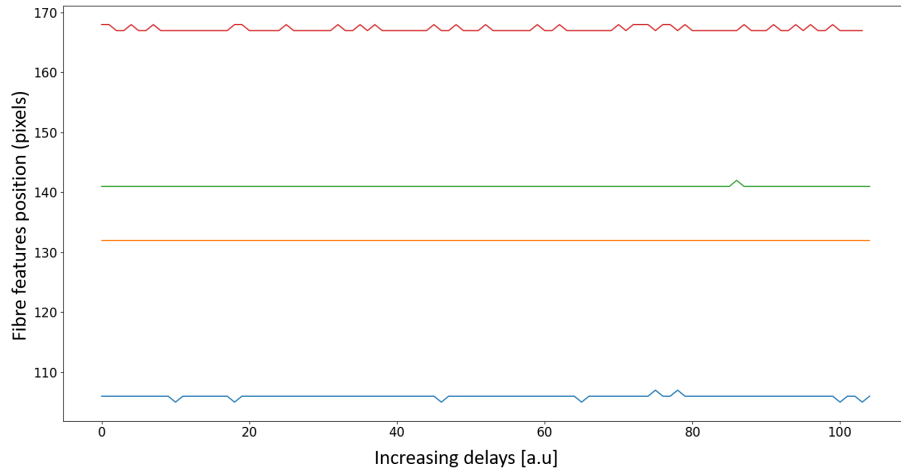
Figure 4.5: This graph shows the movement of the recognised edges of the fibre in pixels for a single cross section through the fibre. The time axis comes from the logarithmic supply of delay times triggered from the Arduino uno, starting at delays of 100 μs between images and ending at a 10^5 s delay between the penultimate and final image. The red and blue lines denote the edges recognised as the top and bottom of the fibre cladding respectively - refer to the top left image in 4.4. The green and yellow line similarly represent the top and bottom of the fibre core respectively.

This evidence shows that the prospect of a larger chip hole is feasible and likely would not be detrimental to the experiment. Further testing including heavy blows to the optical bench and directing compressed air at the fibre produced large $z \gg 10\mu$m oscillations. These oscillations were so large that the fibre was seen to move out of the field of view of the microscope entirely (the field of view as seen in figure 4.4) in real time. However, large physical perturbations of that nature would be more than enough to unlock lasers disrupting the experiment regardless. Air currents will of course not be a problem once inside the vacuum chamber, but they do show the behaviour of the fibres at extreme perturbations would pose problems.

4.1.3   Polarisation testing

Implementation of EIT (electromagnetically induced transparency) within the current experimental set-up is an important step towards demonstrating that an atom-photon junction of this structure can be an effective integrated quantum information system. Before adapting the current system to be able to demonstrate EIT in the chip void, we first wanted to decipher the best configuration for our set-up. An important consideration which warranted investigation was the

possibility of fluctuations in polarisation resulting from light traversing the fibre cavity and then re-entering the fibre after passing through the caesium atoms.

As will be seen in the next section, EIT is achieved using a strong control beam, ω_c, and a far weaker signal beam, ω_s, these beams can either be co-propagating or counter-propagating with respect to the optically pumped medium. Ideally, a co-propagating arrangement would be used as it will be insensitive to the velocity distribution of the atomic medium. Conversely, in a counter-propagating system, atomic velocities in the medium will have opposite detuning's for each laser. Manipulation of both beams is required to observe EIT, this becomes problematic when the beams are both co-propagating and only differ by a frequency of about 9 GHz, making physical separation (beam splitter for example) via wavelength selection difficult. This leaves polarisation as the remaining parameter to separate our two beams and allow us to measure the transmission of the signal beam without detecting the probe beam at the same time.

To determine if a co-propagating scheme is feasible, we needed to investigate the potential fluctuations in polarisation that may be introduced by the fibre hole. For testing purposes, a 780 nm wavelength beam provided by a Toptica laser, first passes through a half-wave plate and then a polarising beam cube, see figure 4.6. Tuning of the half-wave plate allowed us to maximise the transmitted beam with a vertical polarisation into a photodiode. Removing the photodiode and using an incoupler, the light was coupled into chip 14, this consisted of a single mode SM800 fibre with a square shaped hole as can be seen in the table 4.1. A coupling efficiency of 21.4% was achieved through this fibre, close to the value achieved in prior testing see figure 4.2. This beam then passed through another half-wave plate followed by a polarising beam cube. By adjusting the half-wave plate to maximise the reflected (horizontal) component and using a photodiode we could measure the unwanted fluctuations in polarisation produced by the fibre and fibre hole.
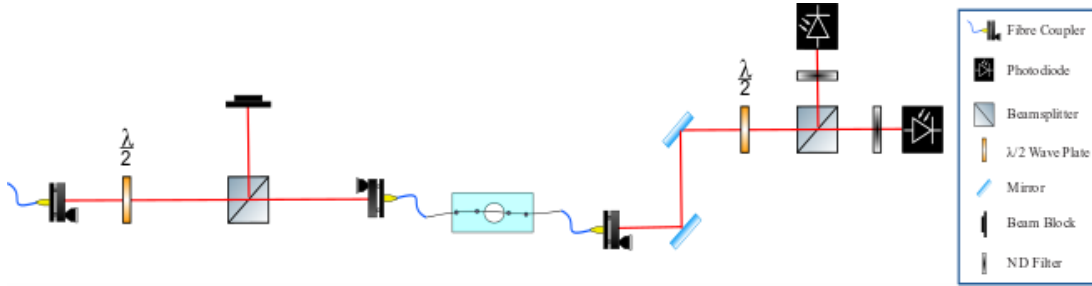
Figure 4.6: Optical set-up diagram for the polarisation fluctuation experiment

The fluctuation data can be seen in figure 4.7. Voltage signal to beam power calibrations were carried out with the respective ND filters used during the experiment to give an accurate conversion. It can be seen that at the longest time scale, the polarisation state leading to power travelling along the unwanted reflected path can oscillate to a maximum of 1.2-1.3% of the total beam power just after passing through the fibre. As we will see in our discussion of EIT later (see section 4.3) the difference in power between the control and signal beam must be significant. A typical control beam is usually at least 10 times as strong as the signal, this would lead to a 12 - 13% power fluctuation at our signal beam according to a 1.2 - 1.3% (see figure 4.7) polarisation fluctuation. This value is not so large that the EIT signal would be totally drowned out but it is large enough to consider counterpropagating over co-propagating. This leads us to the conclusion that a counter-propagating configuration would be the best option for observing EIT in our system. The low temperatures typical of cold atoms experiments utilising MOTs plus sub-Doppler cooling to reach the μK regime should mitigate the velocity sensitivity of the counter-propagating arrangement.
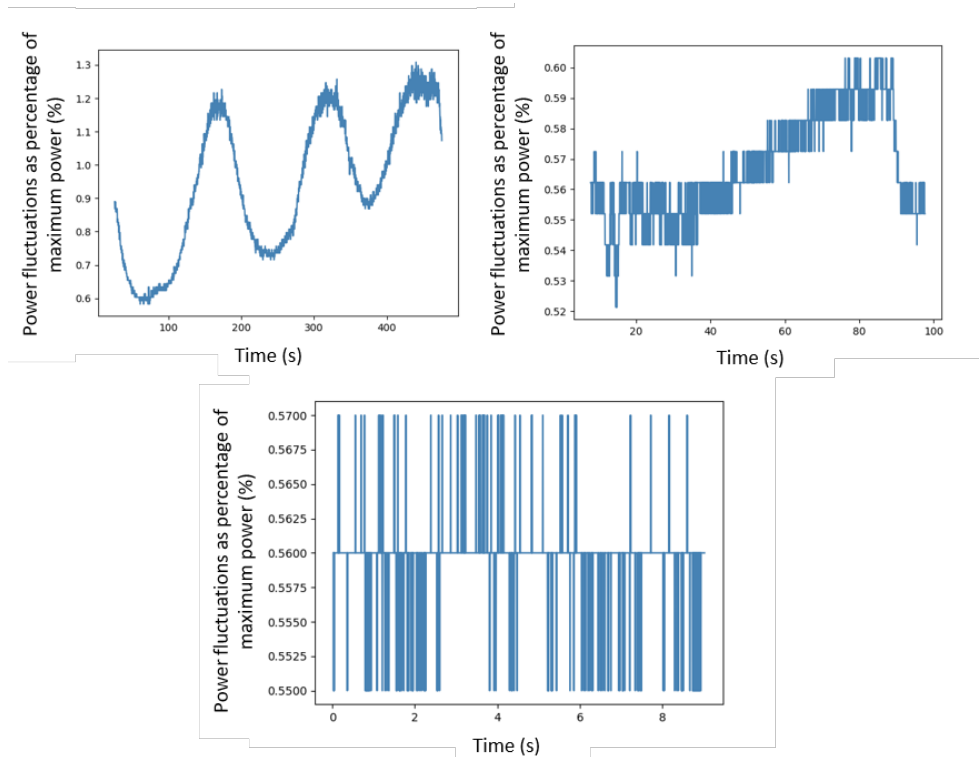
Figure 4.7: These three graphs show the fluctuations in power of the unwanted polarisation coming from the reflected port of the polarising beam cube used to separate the signal and control beam. The values are a percentage of the total input beam power prior to passing through the fibre hole. Each graph shows fluctuations in different time bases, the major fluctuations seen occur on the order of minutes.

4.2   Chip testing

In the short-term we wish to improve our fibre-hole scheme by introducing shaped holes specifically to reduce losses as seen in section 4.1.1. In the long term however, the goal is to use the same experimental scheme but replacing the fibres for chips integrated with both multiple waveguides and through-holes in which we can introduce atoms similar to our current system.

The first step was to experiment with optical chips manufactured to have voids which interrupt the integrated waveguides and to measure what magnitude of coupling can be achieved. Our project partners at the Ferdinand-Braun-Institut (FBH) have kindly provided a chip on which preliminary tests have been carried out. The figure below (figure 4.8) shows both the entirety of the 1x1cm silicon chip mounted for testing and a schematic of the chip design. The top and bottom

singular waveguides are uninterrupted (lacking a hole/void) serving as a reference feature to test coupling of laser light. The rest of the waveguides come in parallel pairs, which contain holes/waveguide-gaps. These holes can be seen in figure 4.9. The schematic also clearly shows two round features which are microresonators, a clear microscope image of one of these resonators can be seen in figure 4.9. The waveguide and resonator architecture are written into the surface of the chip. The base layer of the chip is pure silicon, a silicon oxide (silica) surface layer with a thickness of 2 μm serves as the material in which the waveguides are etched. Figure 4.9 shows clearly the oxide layer containing the waveguide which look like rectangular bars which are cut showing its cross section, this is the end facet of the waveguide where the void has been made in the waveguide. A simple diagram, top-right of figure 4.9, shows the waveguide facet with an area of 2x2 μm^2 suspended on a thin oxide bridge above an etched silicon trench. The isolation of the waveguide helps to reduce leakage of the coupled light into the surrounding structure.
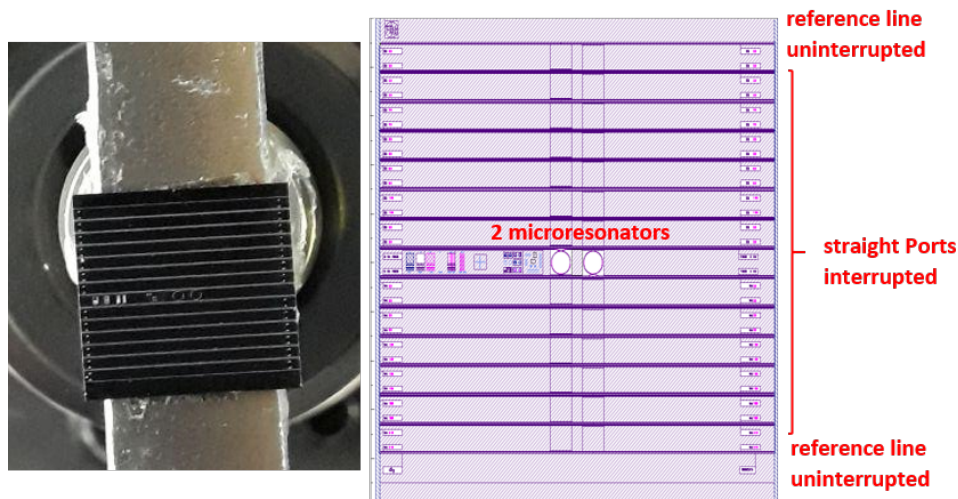

Figure 4.8: A side-by-side view of the chip and its schematic representation. Schematic courtesy of FBH.
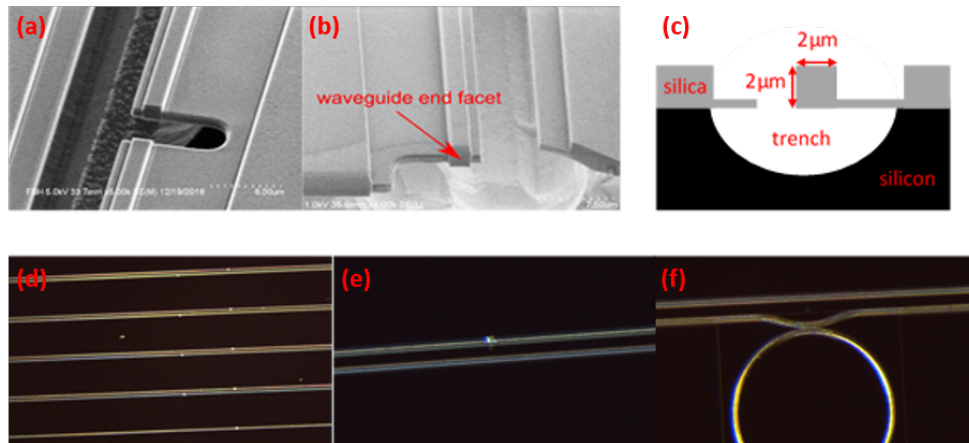
Figure 4.9: Top row of images shows the waveguide gap and its surrounding structure, courtesy of FBH. The right hand image is a diagram showing the cross-sectional structure of the waveguide. The bottom row depicts microscope images of the waveguide holes along parallel pairs of waveguides on our chip as well as a ring resonator.

To attempt coupling of light into a reference waveguide, it was assumed that many degrees of freedom would be necessary due to the small 2x2 μm^2 waveguide facets at the edge of the chip. The set-up implemented can be seen in figure 4.10 along with an image of the 780 nm laser focused and directed onto the chip edge. A typical two mirror scheme fed light into am 11 mm focal length lens with a beam diameter in its focus of 2 μm (calculated from ingoing beam size and lens properties), this beam size was considered good mode-matching to the 2x2 μm^2 waveguide facet. The lens itself was housed inside a 5-axis kinematic mount atop a translation stage allowing movement along the beam path as shown by the green arrows in figure 4.10. This allowed the optimisation of the overlap of the chip edge and the focal plane of the lens. The chip itself is currently mounted atop a piece of aluminium using a small amount of adhesive tape, this set-up is soon to be replaced with a custom made aluminium clamping device which should be vacuum compatible and mountable to our current chamber. The aluminium plate was then epoxied to a post which allowed for height adjustment. This was mounted onto another translation stage allowing the chip to move side to side, which was hoped could make coupling to adjacent waveguides easier once coupling had been achieved in a single waveguide.
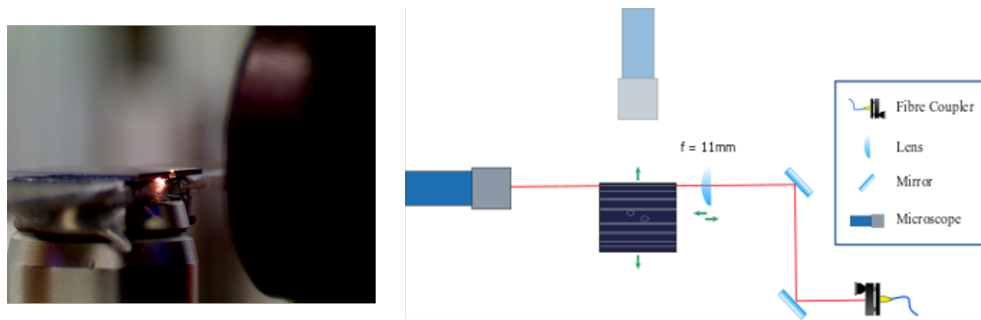
Figure 4.10: On the left we see the beam tightly focused to an expected minimum diameter of 2 μm on the edge of the chip targeting the waveguide entrance facet. The right hand image shows the optical set-up used to attain chip-light coupling. Green arrows represent movement allowed by translation stage for greater control. The microscope position was constantly changed to allow the best possible view to make coupling easier. The microscope aided in the positioning of the focused beam on the waveguide entrance as the beam diameter was extremely small and the 780 nm light is much more visible on the microscope video feed than by the naked eye.

So far, only microscope imaging of scattered light at the exit facet of the coupled chip has been achieved but progress towards a quantitative measurement of the waveguide coupling is ongoing. Figure 4.11 shows the characteristic brightening at the exit facet on the other side of the chip to where light has been successfully coupled (this is easier to see when background light is eliminated). Our colleagues at FBH who have provided the chip have carried out their own tests previously and have data showing the different attenuations at successively longer waveguide gaps as seen in figure 4.12. By translating the chip across the laser focus it can be seen that there is intermittent coupling as we pass each waveguide. However, there are multiple waveguides which have either been damaged or unsuccessfully manufactured, this seems to agree with findings by FBH. To achieve easier coupling we are also investigating the possibility of using lensed fibres to couple directly into the chip waveguides.
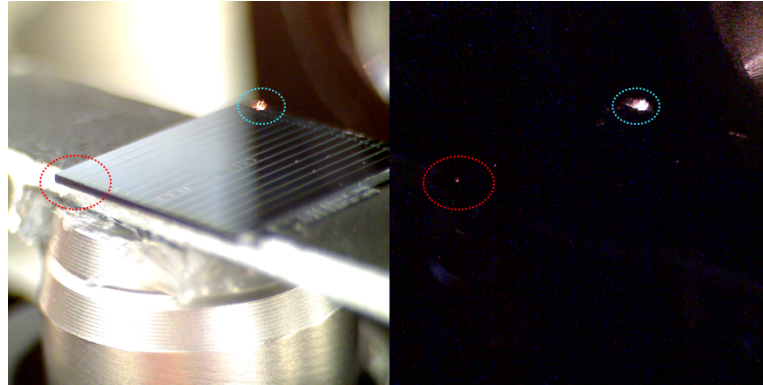
Figure 4.11: Two images showing light leaving the chip at the exit facet of the waveguide. The exit facet of the waveguide is illuminated by dispersed light. The image to the right is under the exact same conditions with the only difference being the reduced background light which allows the exit facet illumination to be observed. Blue outline shows light entering chip at entrance facet, the red outline shows the light at the exit facet.

Although we have not yet quantitatively measured the coupling into the chip waveguides we do have some idea as to how effective the waveguides are. FBH carried out some preliminary tests with their chip before sending them to us. Figure 4.12 shows these results, chip 1 refers to our chip which contained 2x2 μm^2 waveguides whereas chip 2 contained 2x4 μm^2 waveguides where they had used a new technique allowing them to produce 4 μm thick oxide layers rather than 2 μm thick.
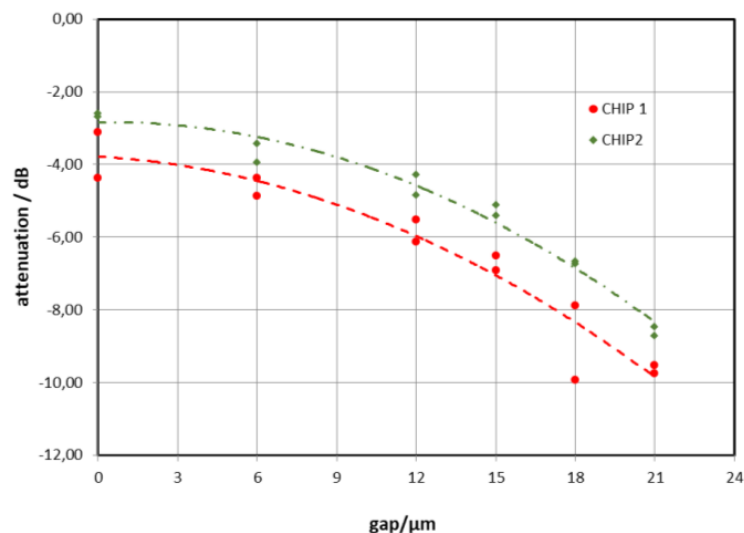
Figure 4.12: FBH chip couplig results for 2x2μm waveguides (chip 1) and 2x4μm waveguides (chip 2).

4.3 EIT background and theory

An important step towards the development of quantum information systems utilising atom-photon interactions is electromagnetically induced transparency or EIT. This method allows for an optically dense medium, such as our caesium gas, to be made transparent at a narrow frequency range by use of a strong control beam, ω_c. A signal beam with frequency, ω_s, is then able to pass through this transparency window. Although this switch-like behaviour[47] due to the quantum mechanical phenomena caused by coherent optical pumping is of interest itself, another phenomena that occurs in tandem is a steep change in the dispersion of the gas. A sharp change in dispersion around the transparency window leads to a phenomenon known as slow light, where the group velocity is significantly reduced, this has potential applications in quantum memory devices[48,49]. Both of these phenomena can be derived from an analysis of the complex susceptibility of the medium using a density operator approach as will be seen later.
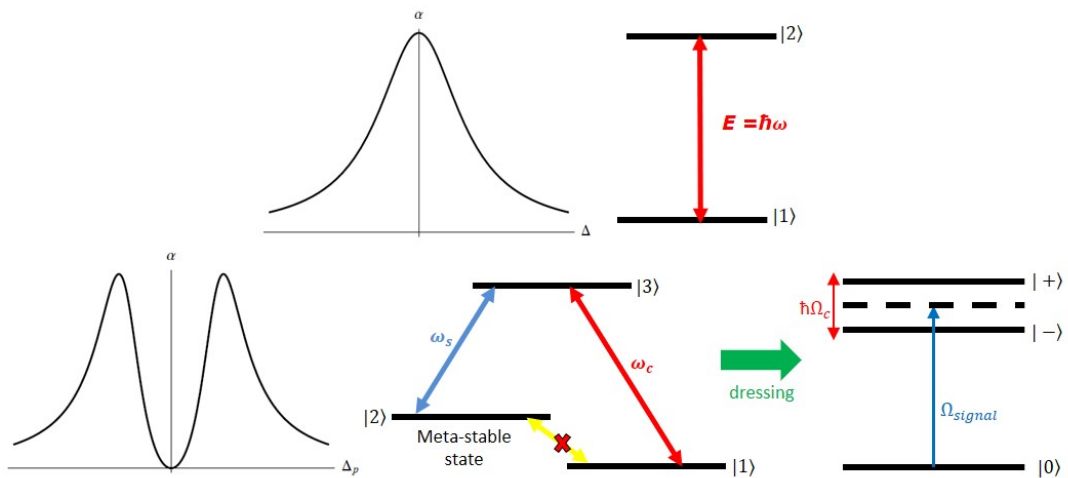
Figure 4.13: Top, we see the simple 2-level atomic system and the associated absorption (α) for resonant radiation (detuning, Δ). Bottom, shows the absorption dip characteristic of EIT on the left; the 3-level scheme with both transitions and the dipole forbidden transition in the middle and the dressed state picture due to the strong control beam, right[50].

We will begin with a more intuitive approach before delving into the mathematical derivation of EIT. In figure 4.13 we see on the top row a typical 2 level atomic system displaying gaussian absorbance, α, on resonance with a light source. The row of images below shows a typical 3 level lambda(Λ)-system. This is the

simplest system in which to display EIT and will be the scheme we shall use in our caesium medium (see figure 4.14). The control beam with Rabi frequency Ω_c, causes a strong atom-photon interaction producing the dressed states $|+\rangle$ and $|-\rangle$ which can be thought to destructively interfere. Between them a maximum transparency region can be seen, indicated by the dashed line. EIT is observed when the much weaker signal beam with Rabi frequency, Ω_s, is scanned across the $|1\rangle$ to $|3\rangle$ transition. Increasing the coupling strength via Ω_c leads to a greater separation $\hbar\Omega_c$ which accordingly widens the frequency window of the induced transparency.
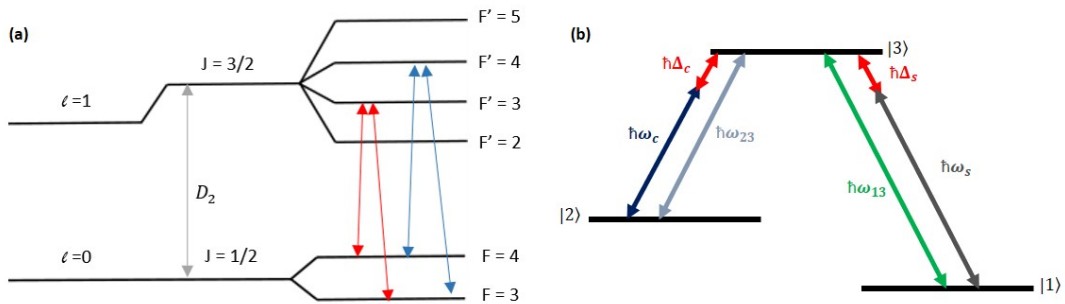
Figure 4.14: In (a) we see the relevant energy level structure for caesium. The blue and red arrows both show two different Λ systems for EIT, either transition can be the control or probe beam. We can see in (b) a Λ system showing the relevant detunings with respect to the transitions and control and probe beam frequencies.

We will begin by examining the bare Hamiltonian for an unperturbed 3-level Λ system[23], where the Hamiltonian is,

$$
H_{atom} = \begin{pmatrix} \hbar\omega_1 & 0 & 0 \\ 0 & \hbar\omega_2 & 0 \\ 0 & 0 & \hbar\omega_3 \end{pmatrix} \tag{4.1}
$$

We can then introduce two perturbing electromagnetic fields with frequencies, ω_c and ω_s, the control and probe beams respectively,

$$
\boldsymbol{E} = \boldsymbol{\mathcal{E}_s} \cos(\omega_s t - \boldsymbol{k_s}.\boldsymbol{r}) + \boldsymbol{\mathcal{E}_c} \cos(\omega_c t - \boldsymbol{k_c}.\boldsymbol{r}) \tag{4.2}
$$

Here $\boldsymbol{E}$ is the perturbing electric field, $\boldsymbol{\mathcal{E}_s}$ is the strength of the probe, $\boldsymbol{\mathcal{E}_c}$ is the amplitude of the control, t is time and $\boldsymbol{k_s}$ and $\boldsymbol{k_c}$ are the wavevectors of each beam. As the atomic radius r $\ll \lambda$ we can neglect the spatial dependence $\boldsymbol{k}.\boldsymbol{r}$. Hence,

$$\boldsymbol{E} = \boldsymbol{\mathcal{E}_s}cos(\omega_s t) + \boldsymbol{\mathcal{E}_c}cos(\omega_c t) \tag{4.3}$$

and our perturbed Hamiltonian becomes,

$$H = H_{atom} + H_{light} \tag{4.4}$$

Here, H_{light} represents the light perturbation and is well approximated to the description of an electric dipole for alkali atoms, which in our system is caesium. Therefore,

$$\boldsymbol{H_{light}} = -q\boldsymbol{E}(t) \cdot \boldsymbol{d}, \tag{4.5}$$

and with the electric charge, q, and the dipole moment, μ, which is defined as,

$$\boldsymbol{\mu} = q\boldsymbol{d}. \tag{4.6}$$

We can rewrite our light perturbed Hamiltonian as,

$$\boldsymbol{H_{light}} = -\boldsymbol{\mu} \cdot \boldsymbol{E}(t) \tag{4.7}$$

where $\boldsymbol{\mu}$ is the dipole moment, q and $\boldsymbol{d}$ are the charge and dipole distance respectively. We define the dipole moment operator as,

$$\hat{\mu} = \mu_{ij}\big(|i\rangle \langle j| + |j\rangle \langle i| \big), \tag{4.8}$$

with the dipole transition element being,

$$\mu_{ij} = \langle i| \hat{\mu} |j\rangle . \tag{4.9}$$

It is then straight forward to see that there are no self transitions allowed hence $\mu_{ij} = 0$ for i = j . Additionally, the assumption is made that the transitions μ_{12} = μ_{21} = 0 due to the transition from $|1\rangle$ to $|2\rangle$ being meta-stable as illustrated in figure 4.13.

The perturbed part of the Hamiltonian can then be written as[50],

$$H_{atom} = -E(t) \begin{pmatrix} 0 & 0 & \mu_{13} \\ 0 & 0 & \mu_{23} \\ \mu_{31} & \mu_{32} & 0 \end{pmatrix} \tag{4.10}$$

Therefore our full Hamiltonian picture is a combination of the bare atom and the light perturbed Hamiltonian such that,

$$H = \begin{pmatrix} \hbar\omega_1 & 0 & -\mu_{13}E(t) \\ 0 & \hbar\omega_2 & -\mu_{23}E(t) \\ -\mu_{31}E(t) & -\mu_{32}E(t) & \hbar\omega_3 \end{pmatrix} \tag{4.11}$$

To see the effect of the perturbing electric field we now have to transform into the interaction picture of the bare atom state. To obtain expressions of the effects we wish to investigate such as the refractive index of the atom cloud and its absorption we must analyse the system as a collection of states. This requires us to transform into the Heisenberg picture in which we observe the change in the expectation values of operators in time, rather than the Schrödinger picture which gives the evolution of individual states in time. Moving forward with this analysis, we choose a rotating basis around the energy eigenstates of the bare Hamiltonian, defining a unitary matrix,

$$\boldsymbol{U(t)} = e^{\frac{iH_{atom}t}{\hbar}} = \begin{pmatrix} e^{i\omega_1 t} & 0 & 0 \\ 0 & e^{i\omega_2 t} & 0 \\ 0 & 0 & e^{i\omega_3 t} \end{pmatrix}. \tag{4.12}$$

By transforming into the Heisenberg picture and applying the rotating wave approximation we produce a new Hamiltonian of the form,

$$\boldsymbol{H} = -\frac{\hbar}{2} \begin{pmatrix} 0 & 0 & \Omega_s e^{-i\omega_{31}t}e^{i\omega_s t} \\ 0 & 0 & \Omega_c e^{-i\omega_{32}t}e^{i\omega_c t} \\ \Omega_s e^{i\omega_{31}t}e^{-i\omega_s t} & \Omega_c e^{i\omega_{32}t}e^{-i\omega_c t} & 0 \end{pmatrix}. \tag{4.13}$$

The Rabi frequencies are defined for the signal and control respectively as[50],

$$\Omega_s = \frac{\mathcal{E}_s|\mu_{13}|}{\hbar} \tag{4.14}$$

$$\Omega_c = \frac{\mathcal{E}_c|\mu_{23}|}{\hbar} \tag{4.15}$$

And the electric dipole operators can be alternatively defined as,

$$\mu_{13} = \mu_{31}^* = |\mu_{13}|e^{i\phi_s} \tag{4.16}$$

$$\mu_{23} = \mu_{32}^* = |\mu_{23}|e^{i\phi_c} \tag{4.17}$$

Where the signal and control beam frequencies are ω_s and ω_c respectively. Relating this to our energy level diagram and the experimental detunings associated with

running an EIT experiment $\omega_s = \omega_3 - \omega_1 - \delta_s = \omega_{31} - \delta_s$ and $\omega_c = \omega_3 - \omega_2 - \delta_c = \omega_{32} - \delta_c$. Now by writing our electric fields in exponential form in our new Hamiltonian and eliminating terms with quick oscillations we transform back into the Schrödinger picture,

$$H = -\frac{\hbar}{2} \begin{pmatrix} 0 & 0 & -\Omega_s e^{i(\omega_s t + \phi_s)} \\ 0 & 0 & -\Omega_c e^{i(\omega_c t + \phi_c)} \\ -\Omega_s e^{-i(\omega_s t + \phi_s)} & -\Omega_c e^{-i(\omega_c t + \phi_c)} & 0 \end{pmatrix}. \qquad (4.18)$$

We must now transform basis once again into the co-rotating, de-tuned basis where $\delta_c = \omega_{32} - \omega_c$ and $\delta_s = \omega_{31} - \omega_s$. This allows us to eliminate the phase and time dependence. The EIT Hamiltonian in a fully rotated basis is found by applying another transformation matrix in the form of,

$$\boldsymbol{U}(t) = \begin{pmatrix} e^{-i\omega_s t} e^{i\omega_{31} t} & 0 & 0 \\ 0 & e^{-i\omega_c t} e^{i\omega_{32} t} & 0 \\ 0 & 0 & 1 \end{pmatrix}. \qquad (4.19)$$

Applying this we obtain the EIT Hamiltonian that describes the 3-level system that can exhibit EIT,

$$\boldsymbol{U}(t)\boldsymbol{H}\boldsymbol{U}^\dagger(t) = \boldsymbol{H}_{EIT} = -\frac{\hbar}{2} \begin{pmatrix} 2\delta_s & 0 & \Omega_s \\ 0 & 2\delta_c & \Omega_c \\ \Omega_s & \Omega_c & 0 \end{pmatrix}, \qquad (4.20)$$

recognising that we now have no time dependent terms inside our Hamiltonian. We can convert our Hamiltonian into a form which will be useful later by the addition of a $2\delta_s$ term multiplied by the identity matrix $\boldsymbol{I}$,

$$\boldsymbol{H}_{EIT} = -\frac{\hbar}{2} \begin{pmatrix} 0 & 0 & \Omega_s \\ 0 & 2(\delta_c - \delta_s) & \Omega_c \\ \Omega_s & \Omega_c & -2\delta_s \end{pmatrix} \qquad (4.21)$$

Interpretation of EIT Hamiltonian

A compact way of expressing the eigenstates of the EIT Hamiltonian is through the use of mixing angles θ and ϕ. In our analysis we have made the detunings of both our signal and control beam equal and small compared to the transitions, $\delta_s = \delta_c = \delta$. We can define,

$$\tan(\theta) = \frac{\Omega_s}{\Omega_c} \tag{4.22}$$

and

$$\tan(2\phi) = \frac{\sqrt{\Omega_s^2 + \Omega_c^2}}{\delta} \tag{4.23}$$

We can solve the determinant of our EIT Hamiltonian and find the associated eigenvalues and eigenstates in terms of the bare atom states using the mixing angles defined above[51].

Calculating these eigenvalues results in,

$$\lambda_0 = 0 \tag{4.24}$$

$$\lambda_- = \hbar\lambda_- = \frac{\hbar}{2}\left(\delta - \sqrt{\delta^2 + \Omega_s^2 + \Omega_c^2}\right) \tag{4.25}$$

$$\lambda_+ = \hbar\lambda_+ = \frac{\hbar}{2}\left(\delta + \sqrt{\delta^2 + \Omega_s^2 + \Omega_c^2}\right). \tag{4.26}$$

And then our eigenstates can be represented in the bare atom basis yielding,

$$|0\rangle = \cos\theta\,|1\rangle - \sin\theta\,|2\rangle \tag{4.27}$$

$$|-\rangle = \sin\theta\cos\phi\,|1\rangle + \cos\theta\cos\phi\,|2\rangle - \sin\phi\,|3\rangle \tag{4.28}$$

$$|+\rangle = \sin\theta sin\phi\,|1\rangle + \cos\theta\sin\phi\,|2\rangle + \cos\phi\,|3\rangle \tag{4.29}$$

It can be seen that the $|0\rangle$ state has no $|3\rangle$ contribution. As both the signal and control beam are resonant toward to $|3\rangle$ transition then it follows that an atom in state $|0\rangle$ has no possibility of being excited to the $|3\rangle$ state and then consequently re-emit a photon via spontaneous emission. For this reason, $|0\rangle$ is referred to as a dark state. Furthermore, $|0\rangle$, $|-\rangle$ and $|+\rangle$ are the so called 'dressed' states which were shown earlier in figure 4.13 for our more intuitive explanation. These states are dressed in the sense that they describe the system of a bare atom interaction with a photon.

Complex Susceptibility

We will now derive the complex susceptibility of an atomic cloud displaying EIT using a different mathematical approach. This will allow us to interpret the interaction differently, revealing the origin of the absorption window of the

atomic cloud and the capability of this system to produce slow light[48,51]. We will do this by applying a density operator on an ensemble of atoms (which is a more realistic scenario than a single atom). We can then derive the susceptibility and find the expressions for the dispersion and absorption characteristics of a gas medium undergoing EIT. We will begin by relating our density operator to the complex susceptibility of an ensemble of atoms. Defining our density matrix by the amplitudes of each state,

$$\rho_{ij} = c_i c_j^*$$
(4.30)

where the index of i and j denote the 3 levels of our Λ system, $i, j = 1, 2, 3$. The diagonal elements of such a matrix represent the populations of each state and the off-diagonal elements the coherences of the system which are a result of the system's response to external electric fields and hence transitions. These off-diagonal terms can be used to define the atomic polarisation, p_{at}, which is induced by a driving external electric field, producing the atomic transitions in the system,

$$p_{at} = \mu_{ij} \rho_{ij}$$
(4.31)

where μ_{ij} gives the dipole matrix element for each transition $|i\rangle \to |j\rangle$. Generalising for a bulk system we simply multiply by the atom number N to find the overall polarisation, P. This can be related to the term we are interested in, that being the susceptibility, χ.

$$P = N\mu_{ij} p_{ij} = \varepsilon_o \chi^{(1)} E$$
(4.32)

The complex susceptibility up to its first order, $\chi^{(1)}$, gives the optical response of a macroscopic medium due to near-resonant light provided by an electric field, E. By using the Rabi frequency $\Omega = \frac{\mu_{ij} E}{\hbar}$ we can introduce our density matrix and hence relate our atomic transitions directly to the susceptibility of the atomic ensemble,

$$\chi^{(1)} = \frac{N}{\varepsilon_o \hbar} \frac{\mu_{ij}^2}{\Omega} \rho_{ij}.$$
(4.33)

The complex susceptibility is related to the refractive index by,

$$n = \sqrt{1 + \chi^{(1)}} \approx 1 + \frac{\chi^{(1)}}{2}.$$
(4.34)

The real and imaginary parts of the refractive index are defined as $n = n_r + i\kappa$. Where n_r is the real part and κ is the imaginary part and is related to the absorption aspect of the susceptibility. The absorption coefficient, α, is related to κ by $\kappa = \frac{\alpha c}{2\omega}$, where ω gives the frequency of the applied electric field and c is the speed of light. Hence we can relate our density matrix and therefore atomic transitions with the real and imaginary part of the complex susceptibility. This provides expressions for the refractive index (n_r) and absorption (α) of the optical medium respectively.

$$n_r = 1 + \frac{1}{2}\text{Re}[\chi^{(1)}] = \frac{N\mu_{ij}^2}{2\varepsilon_o \hbar \Omega_{ij}} Re[\rho_{ij}] + 1 \tag{4.35}$$

$$\alpha = \frac{\omega}{c}\text{Im}[\chi^{(1)}] = \frac{N\mu_{ij}^2 \omega}{\varepsilon_o \hbar \Omega_{ij} c} Im[\rho_{ij}] \tag{4.36}$$

Applying the density matrix

We start by applying the density matrix to our EIT Hamiltonian. The density matrix can be represented explicitly in components as,

$$\rho = \begin{pmatrix} \rho_{11} & \rho_{12} & \rho_{13} \\ \rho_{21} & \rho_{22} & \rho_{23} \\ \rho_{31} & \rho_{32} & \rho_{33} \end{pmatrix}. \tag{4.37}$$

Recalling our EIT Hamiltonian which was derived earlier in equation 4.21,

$$\boldsymbol{H}_{EIT} = -\frac{\hbar}{2} \begin{pmatrix} 0 & 0 & \Omega_s \\ 0 & 2(\delta_c - \delta_s) & \Omega_c \\ \Omega_s & \Omega_c & -2\delta_s \end{pmatrix} \tag{4.38}$$

With our density matrix and EIT Hamiltonian we can apply the von Neumann equation,

$$\partial_t \hat{\rho} = \frac{i}{\hbar}[\hat{\rho}, \hat{H}_{EIT}] \tag{4.39}$$

this allows us to describe the time evolution of the density operator $\hat{\rho}$. By completing the commutation relationship using the defined matrices, we arrive at the optical Bloch equations, which describe the coherences (off-diagonal terms). These represent the response to a driving electric field on the atomic state,

$$\frac{d}{dt}\rho_{12} = (i/2)\Omega_s\rho_{32} - (i/2)\Omega_c\rho_{13} - i(\delta_c - \delta_s)\rho_{12} \tag{4.40}$$

$$\frac{d}{dt}\rho_{13} = \Omega_s(\rho_{33} - \rho_{11})(i/2) - (i/2)\omega_c\rho_{12} + i\delta\rho_{s13} \tag{4.41}$$

$$\frac{d}{dt}\rho_{23} = \Omega_c(\rho_{33} - \rho_{22})(i/2) - (i/2)\omega_s\rho_{21} + i\delta\rho_{c23} \tag{4.42}$$

The Bloch equations also describe the population at each atomic level (diagonal terms),

$$\frac{d}{dt}\rho_{11} = \Omega_s(\rho_{31} - \rho_{13})(i/2) \tag{4.43}$$

$$\frac{d}{dt}\rho_{22} = \Omega_c(\rho_{32} - \rho_{23})(i/2) \tag{4.44}$$

$$\frac{d}{dt}\rho_{33} = \Omega_s(\rho_{13} - \rho_{31})(i/2) + \Omega_c(\rho_{23} - \rho_{32})(i/2) \tag{4.45}$$

To progress further we must introduce the Lindblad equation to account for spontaneous decay and dephasing[52]. We will take the main results[48,51] from the application of the Lindblad equation and define our decay and dephasing terms outright to reduce the amount of mathematical derivation, which is outside the scope of this thesis[53]. Our corresponding Lindblad operators ($\hat{L}_{ij}$) and decay terms (Γ) become,

$$\hat{L}_{13} = |1\rangle\langle3|, \quad \gamma = \Gamma_{31} \tag{4.46}$$

$$\hat{L}_{23} = |2\rangle\langle3|, \quad \gamma = \Gamma_{32} \tag{4.47}$$

$$\hat{L}_{22} = |2\rangle\langle2|, \quad \gamma = \gamma_2 \tag{4.48}$$

$$\hat{L}_{33} = |3\rangle\langle3|, \quad \gamma = \gamma_3 \tag{4.49}$$

We simplify the dephasing and decay terms to produce[52],

$$\Gamma_3 = \Gamma_{31} + \Gamma_{32} \tag{4.50}$$

$$\gamma_{32} = \Gamma_{31} + \gamma_3 + \gamma_2 \tag{4.51}$$

$$\gamma_{31} = \Gamma_3 + \gamma_3 \tag{4.52}$$

$$\gamma_{21} = \gamma_2 \tag{4.53}$$

The application of the Lindblad equation leads to our new optical Bloch equations that now take into account spontaneous emission and dephasing effects. The Bloch Equations 4.40, 4.41 and 4.42 now become,

$$\frac{d}{dt}\rho_{12} = 0 = (i/2)\Omega_s\rho_{32} - (i/2)\Omega_c\rho_{13} - i(\delta_c - \delta_s - (i/2)\gamma_{21})\rho_{12} \tag{4.54}$$

$$\frac{d}{dt}\rho_{13} = 0 = -(i/2)\Omega_s - (i/2)\Omega_c\rho_{12} + i(\delta_s + (i/2)\gamma_{31})\rho_{13} \tag{4.55}$$

$$\frac{d}{dt}\rho_{23} = 0 = -(i/2)\Omega_s\rho_{21} + i(\delta_c + (i/2)\gamma_{32})\rho_{23} \tag{4.56}$$

We concentrate on the ρ_{13} term as this relates to the signal beam that selects the $|1\rangle \rightarrow |3\rangle$ transition and hence the EIT signal. Equations 4.54, 4.55 and 4.56 contain multiple assumptions from our starting Bloch equations. These assumptions deal with the complicating issue of the time dependence of the original Bloch equations. We first assume that the strong pumping beam known as the control beam pumps most of the atoms from state $|2\rangle$ to $|3\rangle$. These states then spontaneously decay into the ground state $|1\rangle$. And so we can make the simplification that the population of states as defined by the density matrix $\rho_{11} \approx 1$ and states $|2\rangle$ and $|3\rangle$ are depleted such that $\rho_{22} \approx \rho_{33} \approx 0$. We can use the rotating wave approximation to eliminate the first term in equation 4.54 as it becomes a second order term as a consequence of $\rho_{32} \approx \Omega_s$. Substituting the equation for $\frac{d}{dt}\rho_{12}$ into $\frac{d}{dt}\rho_{13}$ and rearranging for the parameter we are interested in we find,

$$\rho_{13} = \frac{\Omega_s(2\Delta + i\gamma_{21})}{\Omega_c^2 - (2\delta_s + i\gamma_{31})(2\Delta + i\gamma_{21})} \tag{4.57}$$

where we have defined the detuning as $\Delta = \delta_s - \delta_c$. By now inserting this into our equation for the complex susceptibility we defined earlier (equation 4.33) we arrive at,

$$\chi^{(1)} = \frac{2(2\Delta + i\gamma_{21})}{\Omega_c^2 - (2\Delta + i\gamma_{21})(2\delta_s + i\gamma_{31})} \frac{N\mu_{13}^2}{\varepsilon_o\hbar} \tag{4.58}$$

Finally, by using equations 4.35 and 4.36 we arrive at our expressions for the refractive index and absorption coefficient of our optical medium.

$$n = \frac{N|\mu_{13}|^2}{\varepsilon_o\hbar} \frac{2\Delta(\Omega_c^2 - 4\delta_s\Delta) - 2\gamma_{21}^2\delta_s}{|\Omega_c^2 - (2\delta_s + i\gamma_{31})(2\Delta + i\gamma_{21})|^2} + 1 \tag{4.59}$$

$$\alpha = \frac{N|\mu_{13}|^2 \omega_s}{\varepsilon_o \hbar c} \frac{8\Delta^2 \gamma_{31} + 2\gamma_{21}(\Omega_c^2 + \gamma_{21}\gamma_{31})}{|\Omega_c^2 - (2\delta_s + i\gamma_{31})(2\Delta + i\gamma_{21})|^2} \tag{4.60}$$

Both expressions above are unwieldy and do not give an immediate physical understanding of the system, they do however, give extremely important results. Namely, expressions for the absorption and dispersion relations seen in a medium undergoing EIT, these are the phenomena mentioned previously which have applications in quantum information systems. We can see in figure 4.15 first the real part of the complex susceptibility, which gives us the relationship between the refractive index and the detuning of our signal beam δ_s. The dashed line represents a normal 2-level system lacking the control beam. The solid line represents the 3-level EIT system where the control beam is applied. It can be seen that when the control beam is applied an extremely steep gradient in the refractive index is produced at a small frequency window around resonance. It is this response that is responsible for the phenomenon of slow light which is of interest for quantum information systems. The group velocity of light can be related to the refractive index such that [51],

$$v_{group} = \frac{d\omega_s}{dk_s}\bigg|_{\delta_s=0} = \frac{c}{n + \omega_s \frac{dn}{d\omega_s}} \tag{4.61}$$

The second graph in figure 4.15 shows the relationship between imaginary part of the susceptibility and the signal beam's detuning. For the simple 2-level system we see the familiar Lorentzian absorption centered around the zero detuning point as would be expected. However, when the control beam is used we see the characteristic dip in the absorption at resonance for the signal beam. The width of this window of transparency is dependent upon the strength of the control beam, Ω_c. This behaviour is what is known as electromagnetically induced transparency and it is due the quantum interference of excitation pathways as has been laid out in this section.
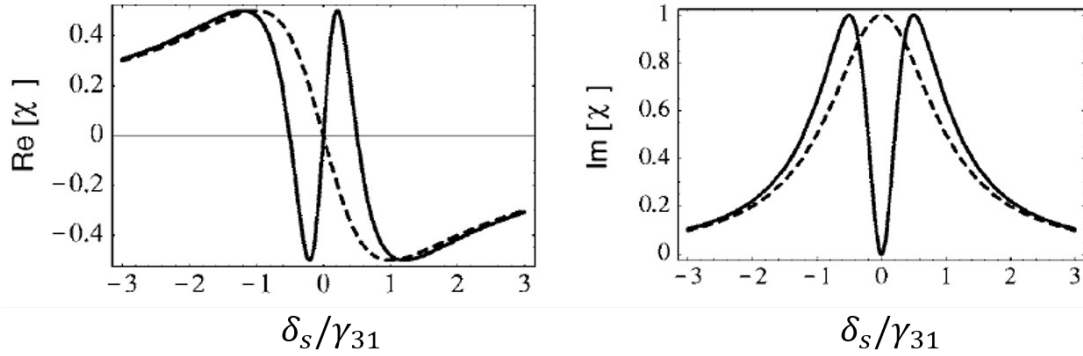
Figure 4.15: Here we see the real and imaginary parts of the complex susceptibility plotted separately. Dashed lines represent a simple 2-level system and solid lines represent a 3-level EIT system with an applied control beam. The familiar absorption EIT signal is easily identified on the right. The imaginary component however shows a steep dispersion relationship at the signal beam resonance. Around this resonance the group velocity of light is significantly slowed, this slow light phenomenon has exciting potential for quantum information systems[48,49]. Figure adapted from M. Fleischhauer et al[51].

4.3.1 Initial EIT data

Before attempting EIT utilising the more complex fibre-chip configuration, the necessary control and signal beams were set up to carry out EIT within a room temperature caesium vapour cell, see figure 4.17. The decision to use a co-propagating configuration was made due to the velocity sensitivity of the atoms. A counter-propagating set-up would make an EIT signal very difficult to observe in a room temperature vapour. The polarisation limitations from section 4.1.3 should not be too much of a problem as we only want to observe EIT in a room temperature caesium cell as a proof of concept. When we reach the stage where we want to apply this technique within the fibre void on cold atoms it will be necessary to use a counter-propagating beam configuration otherwise it will be difficult to remove the control beam from the beam path before reaching the SPCM. The much reduced motion of the atoms in a cooled caesium cloud will mitigate the velocity sensitivity of a counter-propagating system.

The results from this experiment can be seen in figure 4.16. The blue curve shows the Doppler valley and the atomic transition peaks without the control beam applied and only the signal beam as a probe. The green curve shows the system with the control beam turned on. The characteristic intensity peak can be seen on the far right transition showing that the signal beam is passing through the caesium medium via EIT. The possible Λ schemes allowed by the selection

rules with respect to the internal atomic structure of caesium were shown at the beginning of this section, see figure 4.14(a). Of these we selected the $|4\rangle \rightarrow |4'\rangle$ pathway for the control beam in the set-up and the $|3\rangle \rightarrow |4'\rangle$ to act as our signal beam. This is represented by the blue transition arrows in figure 4.14(a). For this configuration a 0.8mW control beam and 0.12mW signal beam were used. The EIT signal beam (table 3.1) is supplied by a newly built ECDL laser which is situated on the isolated optical bench. The control beam is supplied by the new ref laser which is situated on the optical bench with the main experimental chamber. The beams are mixed before and separated after passing through the optical medium via polarisation beam splitters. These beams are then measured using photo-detectors. How these beams look with respect to the overall atomic structure including their detunings see figure 3.5 (orange and purple arrow for the signal and control beam respectively). An AOM in the path of the control beam allows very fast on/off switching of the EIT medium providing a gate-like effect.
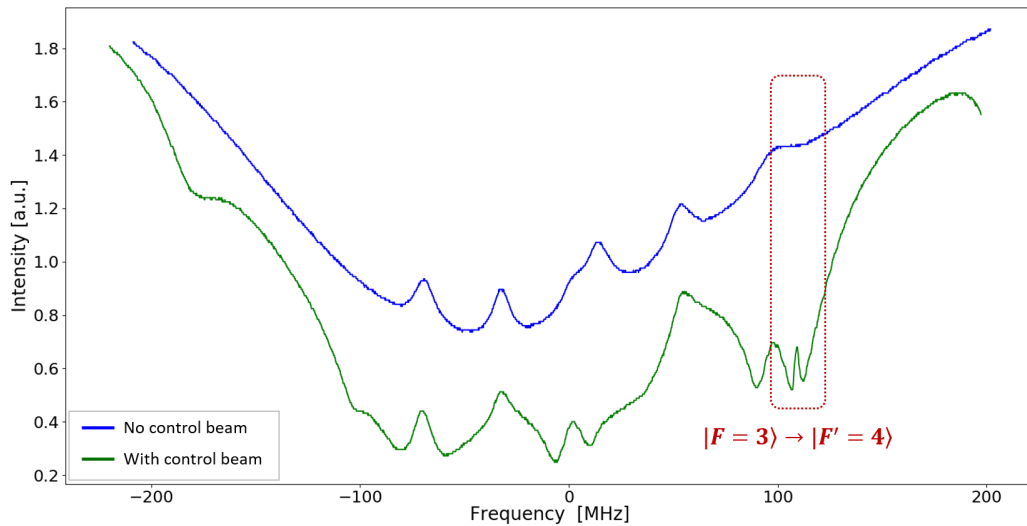
Figure 4.16: Graph showing switching on and off EIT via the control beam. The right hand side of the graph shows a small peak in the intensity of the signal beam. This indicates the transparency of the optical medium to the signal beam which is induced via EIT. This behaviour is seen in the green curve which represents the case where the control beam has been applied. The peak occurs at the F' = 4 transition and has been highlighted by a red window which encapsulates the same frequency band for both the non-control beam and control beam cases.
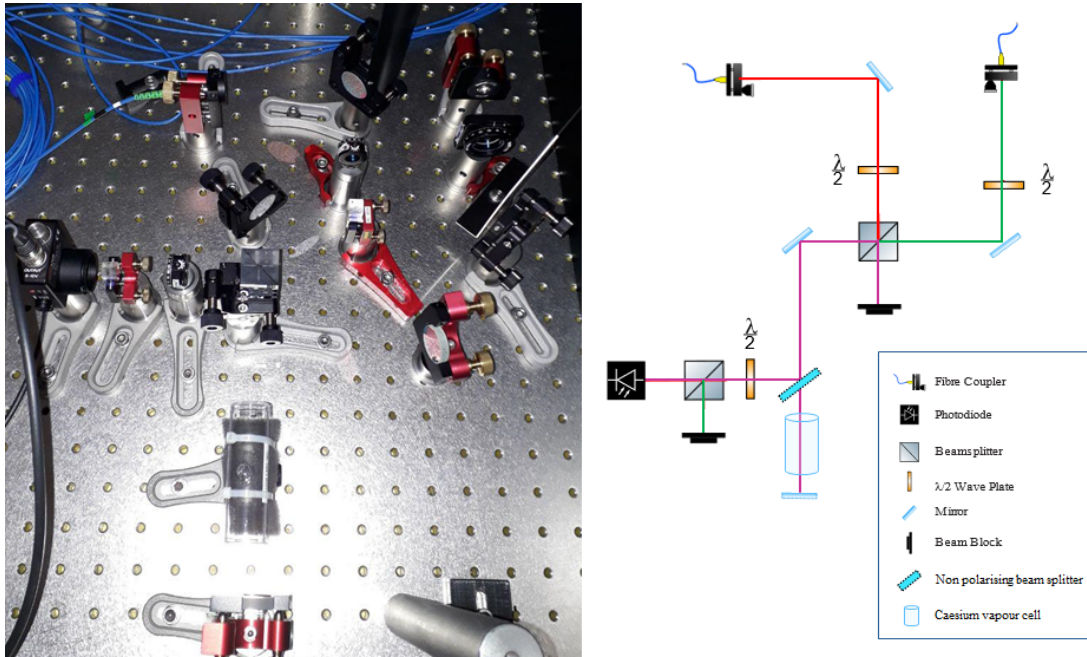
Figure 4.17: Image of the optical table showing the set-up for co-propagating EIT in a caesium vapour cell at room temperature. The same polarisation beam splitter is used to both mix and separate the control and signal beam after performing a double pass through the vapour cell using a retro-reflecting mirror. Right image shows a schematic representation of the set-up.

Chapter 5

Conclusions and future steps

This thesis has detailed the work towards improving a novel atom-photon interface. We have successfully explored the fibre hole geometry to arrive at a good solution for our fibre replacement in future iterations of the experiment. Additionally, we have seen that the measurements of the fibre transmissions with laser-drilled holes matches the theory as presented in work from inside the research group[44]. We have experimentally verified that convex hole shapes give the greatest light transmission followed by square and then circular in agreement with[44]. We have also identified good candidates for future introduction into the chamber from this first batch of laser-drilled fibres. As we now have a better understanding of the effects of hole geometry it will be possible in the future to acquire more fibres and optimise the transmission further e.g. by including anti-reflection coatings or via surface smoothing through heating. The results may also be important for the more complex waveguide chip, as the waveguide gap's geometry could be manipulated similarly to our fibre experiment to maximise transmission.

The work presented here has also shown the inherent mechanical stability of our fibre-chip assembly, this bodes well for its future applications. The influence of the hole on the polarisation of the light was characterised and the polarisation shows only a relatively small drift over time. We calculated that this drift is not significant enough to prevent us from realising EIT in our experimental system. Furthermore, an initial EIT experiment has been carried out in a caesium vapour cell and the prospect of establishing this phenomenon inside the main experiment is imminent. Finally, preliminary characterisation of the silica on silicon waveguide chip which includes waveguide gaps and ring resonators was

carried out. This was done with the intention of introducing a later generation of this chip type into the main experimental system.

In this final part I will outline the future steps that are currently planned to take the atom-photon interface forward. I will also address the results and findings from previous sections as these will inform the decisions made on future research activities.

5.1   Fibre development

As seen in section 4.1.1, the best candidate for the next experiments and insertion into the chamber is chip 4, a single mode 780 HP bare fibre with a convex laser drilled hole. This should benefit us with an almost doubled transmission from the current transmission of 20%. Another future task will involve the re-measurement of the bare fibres without holes. As mentioned in section 4.1.1 and seen in table 4.1, the correction values for the intact fibres must have been too low and hence gave a correction to the drilled fibres which brought them over 100% transmission. Fortunately this is a relatively simple task as the intact fibres are a good deal more robust than the drilled fibres. A final idea to explore the drilled holes further is to introduce post-production optimisation of the fibre holes. This would entail heating of the fibre holes to potentially smooth out surface roughness left by the laser drilling process. This roughness is thought to be the most likely reason for the discrepancy between the theoretical values[44] as compared to the measured values. Another simple experiment would be to introduce small quantities of index matching fluid to the fibre hole and measuring the instantaneous effect on the transmission.

5.2   Chamber rearrangement

A simple to explain but work-intensive task to carry out in the future is the rotation of the Vacuum chamber by 90°. This should increase the effectiveness of the dipole trap as we are currently pushing atoms up against gravity using the axial intensity gradient of the dipole trap which is far weaker than the radial gradient. By rotating the chamber we change the alignment of the dipole beam to horizontal and so we will be using the radial confinement against gravity rather

than the axial.

5.3 Chip design

Moving forwards, we ideally wish to mount a photonic chip with integrated waveguides and waveguide-gaps into the chamber. The current chip supplied by FBH meets these criteria however an important requirement of a potential photonic chip, if it were to work similarly to the current fibre-hole configuration, is that the chip needs to have a through-hole at the site of the waveguide gap. This through-hole would ideally be wide enough to allow passage of the dipole trap beam and hence allow us to introduce cold caesium atoms to create the atom-photon junction. This is no small feat and FBH are currently working towards a solution. Figure 5.1 (a) and (b) shows the processing of one of these through holes at the waveguide gap site at two different stages of completion. These results are promising and have taken place rapidly. Another advantageous aspect of the chip design is the fast turn over between the design and production of a new chip. The latest development is the prospect of introducing these holes on circular resonators much like the resonators already seen on the current chip in figure 4.8 and 4.9. A diagram of such a resonator can be seen in figure 5.1(c), showing different possible sites on the resonator for a hole. The final chip design aspect currently under investigation is the potential of using a material transparent to our MOT beams to alleviate some of the geometric constraints on our system if we were to use a silica on silicon chip[54]. A potential candidate material is sapphire, however it is unknown currently if this material can be compatible with the current processing techniques employed by our chip provider, FBH.
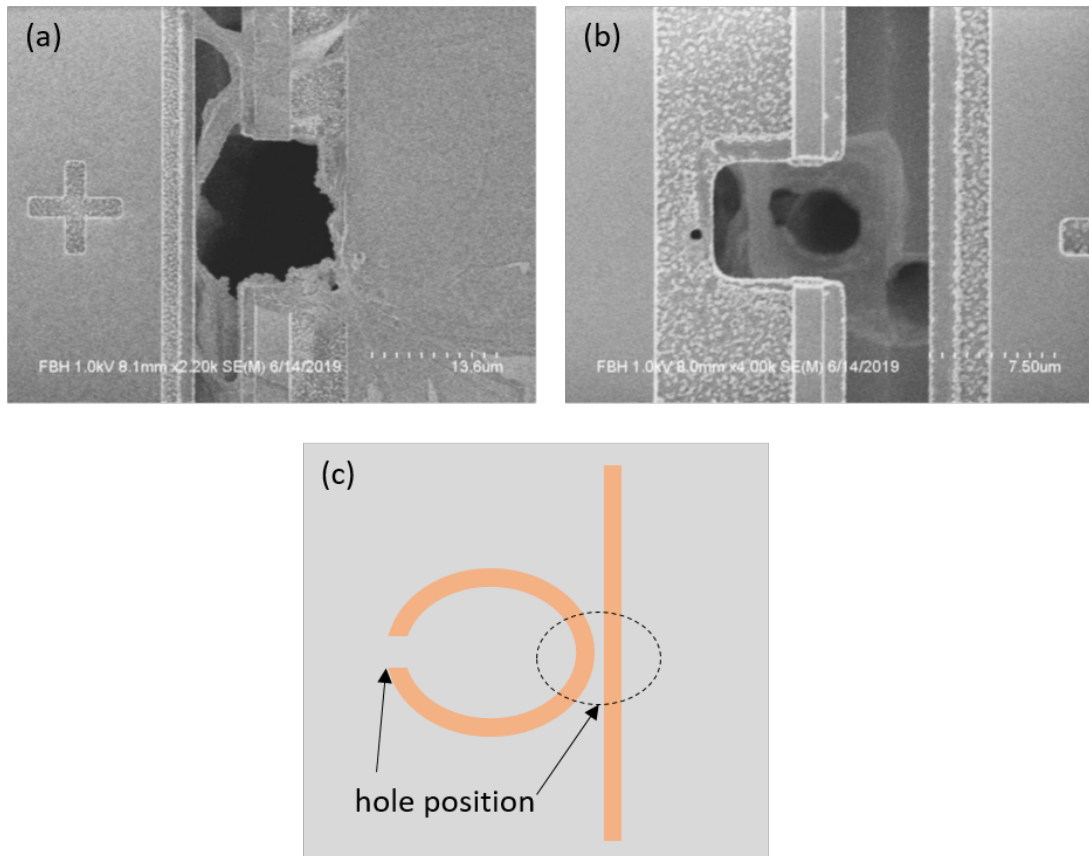
Figure 5.1: Microscope images (a) and (b) courtesy of FBH show their through hole processing in action. The diagram (c) shows a proposed hole-containing ring resonator with the dotted circle showing the other area where a hole could be introduced.

Bibliography

[1] Chu, S., Hollberg, L., Bjorkholm, J.E., Cable, A. and Ashkin, A., 1985. "Three-dimensional viscous confinement and cooling of atoms by resonance radiation pressure". *Physical review letters*, 55(1), p.48.

[2] Anderson, M.H., Ensher, J.R., Matthews, M.R., Wieman, C.E. and Cornell, E.A., 1995. "Observation of Bose-Einstein condensation in a dilute atomic vapor". *Science*, 269(5221), pp.198-201.

[3] Raab, E.L., Prentiss, M., Cable, A., Chu, S. and Pritchard, D.E., 1987. "Trapping of neutral sodium atoms with radiation pressure". *Physical Review Letters*, 59(23), p.2631.

[4] Geiger, R., Ménoret, V., Stern, G., Zahzam, N., Cheinet, P., Battelier, B., Villing, A., Moron, F., Lours, M., Bidel, Y. and Bresson, A., 2011. "Detecting inertial effects with airborne matter-wave interferometry". *Nature communications*, 2(1), pp.1-7.

[5] Hees, A., Guéna, J., Abgrall, M., Bize, S. and Wolf, P., 2016. "Searching for an oscillating massive scalar field as a dark matter candidate using atomic hyperfine frequency comparisons". *Physical review letters*, 117(6), p.061301.

[6] Lewenstein, M., Sanpera, A., Ahufinger, V., Damski, B., Sen, A. and Sen, U., 2007. "Ultracold atomic gases in optical lattices: mimicking condensed matter physics and beyond". *Advances in Physics*, 56(2), pp.243-379.

[7] Kuno, Y., Kasamatsu, K., Takahashi, Y., Ichinose, I. and Matsui, T., 2015. "Real-time dynamics and proposal for feasible experiments of lattice gauge–Higgs model simulated by cold atoms". *New Journal of Physics*, 17(6), p.063005.

[8] Laurent, P., Lemonde, P., Simon, E., Santarelli, G., Clairon, A., Dimarcq, N., Petit, P., Audoin, C. and Salomon, C., 1998. "A cold atom clock in absence of gravity". *The European Physical Journal D-Atomic, Molecular, Optical and Plasma Physics*, 3(3), pp.201-204.

[9] Reiserer, A. and Rempe, G., 2015. "Cavity-based quantum networks with single atoms and optical photons". *Reviews of Modern Physics*, 87(4), p.1379.

[10] Van Enk, S.J., Cirac, J.I. and Zoller, P., 1998. "Photonic channels for quantum communication". *Science*, 279(5348), pp.205-208.

[11] Treutlein, P., Hänsch, T.W., Reichel, J., Negretti, A., Cirone, M.A. and Calarco, T., 2006. "Microwave potentials and optimal control for robust quantum gates on an atom chip". *Physical Review A*, 74(2), p.022312.

[12] Duan, L.M., Lukin, M.D., Cirac, J.I. and Zoller, P., 2001. "Long-distance quantum communication with atomic ensembles and linear optics". *Nature*, 414(6862), pp.413-418.

[13] Briegel, H.J., Dür, W., Cirac, J.I. and Zoller, P., 1998. "Quantum repeaters: the role of imperfect local operations in quantum communication". *Physical Review Letters*, 81(26), p.5932.

[14] Vetsch, E., Reitz, D., Sagué, G., Schmidt, R., Dawkins, S.T. and Rauschenbeutel, A., 2010. "Optical interface created by laser-cooled atoms trapped in the evanescent field surrounding an optical nanofiber". *Physical review letters*, 104(20), p.203603.

[15] Chang, D.E., Thompson, J.D., Park, H., Vuletić, V., Zibrov, A.S., Zoller, P. and Lukin, M.D., 2009. "Trapping and manipulation of isolated atoms using nanoscale plasmonic structures". *Physical Review Letters*, 103(12), p.123004.

[16] Bajcsy, M., Hofferberth, S., Balic, V., Peyronel, T., Hafezi, M., Zibrov, A.S., Vuletic, V. and Lukin, M.D., 2009. "Efficient all-optical switching using slow light within a hollow fiber". *Physical review letters*, 102(20), p.203902.

[17] Christensen, C.A., Will, S., Saba, M., Jo, G.B., Shin, Y.I., Ketterle, W. and Pritchard, D., 2008. "Trapping of ultracold atoms in a hollow-core photonic crystal fiber". *Physical Review A*, 78(3), p.033429.

[18] Daly, M., Truong, V.G., Phelan, C.F., Deasy, K. and Chormaic, S.N., 2014. "Nanostructured optical nanofibres for atom trapping". *New Journal of Physics*, 16(5), p.053052.

[19] Metcalf, H.J. and Van der Straten, P., 2007. Laser cooling and trapping of neutral atoms. The Optics Encyclopedia: Basic Foundations and Practical Applications.

[20] Steck, D.A., 2003. Cesium D line data.

[21] Wineland, D.J., Drullinger, R.E. and Walls, F.L., 1978. "Radiation-pressure cooling of bound resonant absorbers". *Physical Review Letters*, 40(25), p.1639.

[22] Phillips, W.D. and Metcalf, H., 1982. "Laser deceleration of an atomic beam". *Physical Review Letters*, 48(9), p.596.

[23] Foot, C.J., 2005. Atomic physics (Vol. 7). Oxford University Press.

[24] Metcalf, H. and Van der Straten, P., Laser cooling and trapping, Springer, New York 1999.

[25] Griffiths, D.J., 2004. Intro. to Quantum Mechanics.

[26] Wineland, D.J. and Dehmelt, H., 1975. "Proposed 1014δv/v laser fluorescence spectroscopy on Tl+ mono-ion oscillator III (side band cooling)". *Bull. Am. Phys. Soc*, 20(4), pp.637-637.

[27] Hänsch, T.W. and Schawlow, A.L., 1975. "Cooling of gases by laser radiation". *Optics Communications*, 13(1), pp.68-69.

[28] Wineland, D.J. and Itano, W.M., 1979. "Laser cooling of atoms". *Physical Review A*, 20(4), p.1521.

[29] Ungar, P.J., Weiss, D.S., Riis, E. and Chu, S., 1989. "Optical molasses and multilevel atoms: theory". *JOSA B*, 6(11), pp.2058-2071.

[30] Kasevich, M., Weiss, D.S., Riis, E., Moler, K., Kasapi, S. and Chu, S., 1991. "Atomic velocity selection using stimulated Raman transitions". *Physical review letters*, 66(18), p.2297.

[31] Lett, P.D., Watts, R.N., Westbrook, C.I., Phillips, W.D., Gould, P.L. and Metcalf, H.J., 1988. "Observation of atoms laser cooled below the Doppler limit". *Physical review letters*, 61(2), p.169.

[32] Wineland, D.J., Dalibard, J. and Cohen-Tannoudji, C., 1992. "Sisyphus cooling of a bound atom". *JOSA B*, 9(1), pp.32-42.

[33] Luiten, O.J., Reynolds, M.W. and Walraven, J.T.M., 1996. "Kinetic theory of the evaporative cooling of a trapped gas". *Physical Review A*, 53(1), p.381.

[34] Ashkin, A., Dziedzic, J.M., Bjorkholm, J.E. and Chu, S., 1986. "Observation of a single-beam gradient force optical trap for dielectric particles". *Optics letters*, 11(5), pp.288-290.

[35] Lang, M.J. and Block, S.M., 2003. "Resource Letter: LBOT-1: Laser-based optical tweezers". *American journal of physics*, 71(3), pp.201-215.

[36] Block, S.M., Blair, D.F. and Berg, H.C., 1989. "Compliance of bacterial flagella measured with optical tweezers". *Nature*, 338(6215), pp.514-518.

[37] Grimm, R., Weidemüller, M. and Ovchinnikov, Y.B., 2000. "Optical dipole traps for neutral atoms". *In Advances in atomic, molecular, and optical physics* (Vol. 42, pp. 95-170). Academic Press.

[38] Jones, M., 2014. "Preparation of Cold Samples of Caesium-133 and Lithium-6 in a Single Apparatus for Bose-Fermi Mixture Experiments" (Doctoral dissertation, University of Nottingham).

[39] Warriar, S., 2014. "Towards an Ultracold Bose-Fermi Mixture of Cesium and Lithium Atoms" (Doctoral dissertation, University of Nottingham).

[40] Paris Mandoki, A., 2015. "A Single Apparatus for the Production of Ultracold Fermionic Lithium and Cold Bosonic Caesium Gases" (Doctoral dissertation, University of Nottingham).

[41] Nute, J., 2016. "A Quantum Integrated Light and Matter Interface" (Doctoral dissertation, University of Nottingham).

[42] Da Ros, E., 2019. "Integrating cold caesium atoms into optical waveguides" (Doctoral dissertation, University of Nottingham).

[43] Ketterle, W., Durfee, D.S. and Stamper-Kurn, D.M., 1999. "Making, probing and understanding Bose-Einstein condensates". arXiv preprint cond-mat/9904034.

[44] Cooper, N., Da Ros, E., Briddon, C., Naniyil, V., Greenaway, M.T. and Hackermueller, L., 2019. "Prospects for strongly coupled atom-photon quantum nodes". *Scientific reports*, 9(1), p.7798.

[45] Kato, S. and Aoki, T., 2015. "Strong coupling between a trapped single atom and an all-fiber cavity". *Physical review letters*, 115(9), p.093603.

[46] Miller, R., Northup, T.E., Birnbaum, K.M., Boca, A.D.B.A., Boozer, A.D. and Kimble, H.J., 2005. "Trapped atoms in cavity QED: coupling quantized light and matter". *Journal of Physics B: Atomic, Molecular and Optical Physics*, 38(9), p.S551.

[47] Mücke, M., Figueroa, E., Bochmann, J., Hahn, C., Murr, K., Ritter, S., Villas-Boas, C.J. and Rempe, G., 2010. "Electromagnetically induced transparency with single atoms in a cavity". *Nature*, 465(7299), p.755.

[48] Muller, M., 2010. "Realization and characterization of a phase locked laser system for coherent spectroscopy of fiber-coupled cesium atoms" Melanie Muller (Doctoral dissertation).

[49] Gouraud, B., 2016. "Optical Nanofibers Interfacing Cold Atoms-A Tool for Quantum Optics" (Doctoral dissertation).

[50] Furman, W.A., 2016. "Electromagnetically Induced Transparency: The Zeeman Method" (Doctoral dissertation, Reed College).

[51] Fleischhauer, M., Imamoglu, A. and Marangos, J.P., 2005. "Electromagnetically induced transparency: Optics in coherent media".*Reviews of modern physics*, 77(2), p.633.

[52] Pyragius, T., Murphy, S., 2014. "Laser Spectroscopy and Electromagnetically Induced Transparency in Caesium vapour" (Master's thesis).

[53] Breuer, H.P. and Petruccione, F., 2002. The theory of open quantum systems. Oxford University Press on Demand.

[54] Longhi, S., 2015. "Supersymmetric transparent optical intersections". *Optics letters*, 40(4), pp.463-466.